Contract No. and Disclaimer:

This manuscript has been authored by Savannah River Nuclear Solutions, LLC under Contract No. DE-AC09-08SR22470 with the U.S. Department of Energy. The United States Government retains and the publisher, by accepting this article for publication, acknowledges that the United States Government retains a non-exclusive, paid-up, irrevocable, worldwide license to publish or reproduce the published form of this work, or allow others to do so, for United States Government purposes.

Complexity in Salt Marsh Circulation for a Semi-enclosed Basin

Jessica Chassereau Sullivan[1], Raymond Torres[1], Alfred Garrett[3], Jackson Blanton[2], Clark Alexander[2], Michael Robinson[2], Trent Moore[2], Julie Amft[2], David Hayes[3]

1. University of South Carolina, Department of Earth and Ocean Science, 701 Sumter Street, Columbia, SC 29208, USA

2. Skidaway Institute of Oceanography, 10 Ocean Science Circle, Savannah, GA 31411, USA

3. Savannah River National Laboratory, Aiken, SC 29808, USA

Key Points:

1. Model results show simultaneous convergent, divergent and rotational flow.
2. All scales of flow illustrate strong temporal and spatial variability.
3. Robust model results arise from high quality DEM and field data.

1. ABSTRACT

We characterize complexity in salt marsh circulation over a 2km^2 basin using field observations, dye tracer and numerical simulations. The marsh bathymetry was created with high precision Global Positioning System surveys to map intertidal creeks greater than 1m wide. Model calibration and validation were quantified, and the model results provide a robust representation of field conditions in that model efficiency varied from 0.82 – 0.99 for pressure and velocity, and 0.36 – 0.83 for dye concentration. Moreover, the overall spatial distribution of simulated dye mimics the distribution observed in aerial photographs. We assessed flow at four spatial scales ranging from 1m – 1,000m, and highlight the temporal and spatial variability of processes that give rise to overmarsh circulation. At times not necessarily linked to the transition between flood and ebb, the current magnitude and direction were highly dynamic, with variations occurring on the order of tens of minutes. Model results show simultaneous flow divergence and convergence, concentrated flow, as well as large-scale rotational flow. Also, all spatial scales show strong differences between flood and ebb pathways, which gives rise to 53% transport of the dye export via overmarsh and intertidal creek flows, and 32% exiting through the central subtidal channel system; 15% remained in the system after five days. Most of the modeled current complexity appears to be set by submergence and emergence of salt marsh topography and geomorphic structure.

Index Terms: 4562, 0442, 1890, 4534

Keywords: Overmarsh circulation, salt marsh topography, numerical modeling, dye transport

2. INTRODUCTION

While conducting fieldwork in a salt marsh one can observe suspended and floating material in transit, and that this material can change speed and direction several times in the course of a tidal inundation. Of course, shifting wind conditions can account for surface water flow complexity, but overmarsh currents can vary substantially without wind effects [*Kjerve et al.*, 1991; *French and Stoddart,* 1992; *Leonard*, 1997; *Allen*, 2000; *Lawrence et al.*, 2004]. Understanding the controls and scales of current complexity in salt marshes or tide influenced wetlands is important because in many cases it strongly influences the distribution of suspended and dissolved nutrients [*Valiela et al.*, 1978], larva distribution [*Kneib*, 1984], and contaminant dispersal [*Nixon,* 1980; *Blanton et al.*, 2010].

Field and numerical studies indicate that the primary controls on salt marsh circulation and associated material redistribution include vegetation drag [*Leonard and Luther*, 1995; *Christansen et al.*, 2000; *Leonard and Reed*, 2002; *Temmerman et al.*, 2005] and topography [*French and Stoddart*, 1992; *Lawrence et al.*, 2004; *Torres and Styles*, 2007; *Chen and Torres*, 2012]. However, the detailed bathymetry or high resolution DEMs necessary for assessing the role of very subtle relief of salt marshes on overmarsh circulation typically are not present, and consequently the role of topography could not be fully evaluated. For example, *Temmerman et al*. [2005] used numerical simulations on a 0.05km^2 salt marsh catchment to assess the interactions of topography, vegetation, and water level fluctuations on spatial variations in flow and sedimentation. Their flow domain was derived from a lidar DEM with 3m point spacing and a vertical accuracy of 0.13m. Hence, effects of depressions and creeks less than 3m wide were

precluded. On the other hand, their model validation showed that the 3m DEM point spacing did not noticeably influence simulation results. In a related study of flow sensitivity to DEMs *McKean et al*. [2014] introduced random errors to a lidar DEM to assess the effects on 2D hydrodynamic simulations in a gravel bed stream, and they also found nominal effects.

Cea and French [2012] investigated the sensitivity of hydrodynamic simulations to uncertainties in bathymetry and bed friction in subtidal, low intertidal, and high intertidal sub-regions of an estuary. In contrast to the studies above, they found a strong response in current velocity to bathymetry, whereas water level fluctuations were more influenced by bed friction. Also, numerical simulations by *Blanton et al*. [2010] successfully replicated tidal driven flows through a salt marsh but their tracer results were not as robust due to tracer retention in the marsh interior. These results led the authors to speculate that salt marsh circulation is highly sensitive to small scale variations in topography, and in particular to the effect of smaller "capillary" creeks or intertidal creeks less than about 1m in width and depth. Taken together, these studies highlight the important point that researchers have yet to characterize the role of small-scale topographic structure on salt marsh circulation.

Here we define overmarsh flow complexity as changes in current direction and magnitude that occur over short time intervals, and we use field observations of dye tracer dispersal and subtidal channel currents, and numerical simulations to understand the temporal evolution of and controls on overmarsh circulation. In particular we simulate salt marsh flood and ebb conditions over a high resolution and high precision salt marsh DEM to help unravel the role of topographic structure in spatial and temporal

variations in salt marsh currents. Modeled pressure, velocity, and dye transport replicate field observations, and we use this information to evaluate complexity in overmarsh circulation at four spatial scales: the whole system or basin (1000m), macro (100m), meso (10m), and micro (1m) scales over a set of tidal cycles with the specific goal of providing a detailed account of basin inundation and drainage by assessing free surface elevation, tracer residence time, water balances and local currents. The assigned length increments of the four spatial scales are not necessarily meant to represent the length of individual flow assessments, but instead were taken to reflect the length scale of the underlying flow processes that we endeavored to highlight in this study.

3. STUDY SITE

The study site is a 2km^2 relatively isolated, section of a larger salt marsh system at 31.96°N, -81.02W°, ~20km south of Savannah, Georgia, USA (Figure 1). The local tidal regime is mixed, semi-diurnal and ebb dominant with a mean tidal range of 2.5m (Figure 2). The basin is semi-enclosed with forested land to the west and south where the forest-marsh edge is defined by a 1m - 3m bluff. The northern border of the study site is Groves Creek a sinuous, ~ 50m-wide subtidal channel that provides a connection between the salt marsh and the Wilmington River to the east (Figure 1).

The neap and spring tidal prisms are $8.11 \times 10^5 m^3$ and $1.76 \times 10^6 m^3$, respectively, based on the DEM volume between high water and low water elevations. The basin flushing-time, the hypothetical time for the exchange of one full basin volume [Equation 4 of *Dyer*, 1973] is 1.12 days and 0.52 days for neap and spring conditions, respectively.

These flushing-time estimates are similar to basins with comparable surface areas, volume, tidal range and tidal prism [e.g. *Abdelrhman,* 2005].

The vegetation is a monoculture of the smooth cordgrass *Spartina alterniflora* (*S. alterniflora*) with spatial variations in density and height dependent on surface elevation [*Kostka*, 2002; *Blanton et al.*, 2010]. For instance, tall form S. *alterniflora* with stem heights that exceed 2m and a density of about 112stems/m^2, grows on the high channel banks and levees. The short form, which typically occurs on the lower marsh platform, has an average stem height of 0.28m, and a stem density of about 446 stems/m^2. The vegetation heights and stem densities are based on clippings taken during a related study.

In order of higher to lower elevations the study area consists of 10% levee, 46% marsh platform, 13% low marsh, 19% intertidal creeks, and 12% subtidal channel. Levees may occur along the subtidal channel and intertidal creeks, and reach 0.75m - 1.30m (NAVD88). The marsh platform is a broad expanse of vegetated, low-relief landscape that forms between 0.45m - 0.74m and has a mean of 0.61m. The low marsh is sparsely vegetated and forms at the heads of intertidal creeks and in some areas form a large depression between 0.21m - 0.44m along an area of marsh east of the terrestrial boundary (Figure 1). Hereafter we refer to this area as the “marsh interior”.

Groves Creek is the main channel, and it is 3.8km along-channel from the furthest reach in the marsh interior to the mouth at the Wilmington River. From there it is 11km to the ocean. Groves Creek maximum depth is -4.50m at the mouth and declines to -0.80m inland; the corresponding bank-to-bank widths are 60m and 10m, respectively (Figure 3). At the site of our dye injection line, 2.2km from the mouth, the width is 35m and maximum depth is 4.0m (Figure 3). At 0.9km upstream of the injection line Groves

Creek splits into three main branches, for convenience called West, Middle, and East, with lengths of 1,100m, 700m, and 500m, respectively (Figure 1).

There are 88 intertidal creeks with mouth elevations ranging from -0.79m - +0.20m. The spacing between creek mouths is ~40m and maximum intertidal creek lengths vary from 10m - 500m. The creek widths range from <1m - 20m. Narrower creeks typically occur in the northern areas of the marsh, across levees. There is a complex network of creeks beginning after the fifth bend in Groves Creek that are connected at the heads by low marsh (Figure 3). This low-lying area provides a connection between the northern and southern marsh interior (Figure 3). A second complex network dissects an area of low marsh in the southeast, hereafter referred to as “dissected marsh” (Figure 1). The longest and deepest intertidal creeks in the basin are along the eastern marsh edge and they provide a direct connection between the marsh interior and the Wilmington River (Figure 1).

The tidal range at Groves Creek varies from 1.54m and 3.20m between neap and spring tides based on tidal oscillations observed at Station 1 (Figure 2). This study took place over a five-day interval from October 31 - November 5, 2010 when the tidal range was 2.1m - 3.2m (Figure 2). Hereafter, we refer to these minimum and maximum amplitudes as "neap" and "spring", respectively. The maximum water elevation during the neap and spring cycles was 0.78m and 1.45m, respectively. Therefore, at neap high tide the depth of water over the marsh platform was about 0.33m. During the spring high tide the water depth over the marsh platform was about 1.0m and the entire basin was submerged.

4. METHODS

4.1 - Field Data

Thirty-two kg of Rhodamine dye was released as a line source applied 80m south of, or "upstream" of Station 2 on November 1st, 2010 (Figure 3) at 15:55 GMT (all time reported hereafter are in GMT), approximately 1.5hrs after low tide. The duration of the dye application was 15 minutes over a single pass across the channel. The amount of dye used was computed to offset the effects of dilution from the tidal prism and preserve measureable dye concentrations in the marsh interior.

We also used a range of instruments that were installed in the subtidal system. The array includes Nortek Aquadopp acoustic Doppler current profilers (ADCP), SBE16 CTDs, ISCO automated dye samplers, and Wetlabs ECO FLRHSB Rhodamine fluorometers all deployed in various combinations at eight stations (Table 1). Automated dye information was augmented by manually collecting water samples from boats (grab samples). All submerged instruments sampled at 10-minute intervals, the ISCO sampling rate was hourly, and the grab-sampling rate varied from 1 – 5 minutes for 2 hours with finer temporal resolution over the 1hr passage time of the plume advance. All station locations are shown in Figure 3 and distances from the line source to the station are reported as along-channel distances. Station 1 was near the channel mouth 1,680m from the dye source. Station 2 had one bank on the forested bluff 80m north of the line source. Stations 3, 4, and 5 were in the East, Middle, and West subtidal branches, respectively. Station 6 was also in the West branch near the southern terrestrial boundary 1,760m from the line source (Figure 3). Station 7 was in the low marsh interior 1,490m east of the line source and 100m north of the southern terrestrial boundary. Station 8 was in the large

intertidal creek along the eastern marsh edge 1,900m east of the dye source (Figure 3). Observed pressure and velocity from Stations 1-6 were used to calibrate the model described in the next section. The dye analyses and results described below include all available data (Table 1). In addition, a series of air photos taken during the experiment were used to qualitatively compare the simulated to observed dye distributions.

Trimble R6 GPS receivers were used to collect high-resolution topography three ways, by surveying points individually, with a SonarMite echo sounder for intertidal creeks, and with a Simrad multibeam system for Groves Creek. The higher elevations were surveyed at low water, and the soundings for intertidal creeks were made from a small motorized craft at high water. The survey consisted of 241 individual missions over 169 field days in 2010 and 2011 resulting in 1.6×10^5 points with spacing ranging from 0.25m – 5m. RTK corrections were received through a VRS (Virtual Reference Station) operated by eGPS Solutions, Inc. reporting 0.02m horizontal and 0.02m vertical accuracies when connected to the internet via cellular telephone. ArcGIS software was used to linearly interpolate the survey data onto a 1m DEM for use in hydrodynamic simulations with Delft3D (Figure 3).

4.2 – Model Description, Settings and Calibration

The Delft3D simulation package consists of integrated modules which interact to compute water currents, water quality, and particle transport for user specified bathymetry, roughness, horizontal eddy viscosity, and dispersion coefficients. The standard hydrodynamic module is Delft3D FLOW and it is essential for modeling flow phenomena where horizontal length scales are significantly larger than the vertical [*Lesser et al.*, 2000]. Delft3D is well suited for this study and has been applied

successfully to salt marsh research in several different locations [*Temmerman et al.*, 2005, *Marciano et al.*, 2005, *Bouma et al.*, 2007 and *Fagherazzi et al.*, 2014]. Computation of unsteady shallow-water flow is determined through the horizontal momentum equation, the continuity equations, and transport equations. Bed roughness and horizontal eddy viscosity are both user defined and typically follow from calibration. Delft3D FLOW uses a finite-difference approach to compute water level and depth averaged velocity at each node. The FLOW output is subsequently coupled to the PART module to simulate the advection and diffusion of particles. Delft3D PART accounts for the random spreading of particles through the horizontal dispersion coefficient H_D defined by Equation 1 [*Csanady*, 1973]

$$H_D = at^b \quad (1)$$

where t is the age of the particle, and a and b are coefficients that emerge from the model calibration. For 2D flows the user must also specify a roughness length parameter, typically through calibration, which is used to calculate the logarithmic velocity profile.

The simulations were conducted on a grid with uniform 1m horizontal spacing giving 5×10^6 computational nodes. The domain was closed to the west and south along the terrestrial border, and closed to the north along the outer bank of Groves Creek. The domain was open to flow along the eastern boundary defined by the water level time series from Station 1. The model assigns positive and negative values to flows in the direction of increasing or decreasing X or Y, respectively. In this study, the origin of the computational domain is to the left of the open flow boundary. Therefore, flood velocities are negative and ebb velocities are positive. The geographic orientation of the channel at Station 5 introduces ambiguity into the direction of flood and ebb (Figure 3). Therefore,

all velocities at Station 5 were multiplied by -1 to ensure that flood velocities in all cases were negative.

The model was calibrated with pressure and velocity data. The horizontal eddy viscosity was set to 0.0005m^2/s [*Temmerman, et al.*, 2005] and bottom roughness was applied as a calibration variable by adjusting Manning's n values for vegetated (> 0.20m) and unvegetated (≤ 0.20m) marsh, constrained by the range of n values for salt marshes (Table 2), and by comparing results to observations. The model efficiency [ME, after *Nash and Sutcliffe*, 1970] was calculated with the entire time series record to guide model validation and to determine optimal values for Manning's n as described below.

$$ME = 1 - \frac{\sum_{t=1}^{T} (OBS(t) - SIM(t))^2}{\sum_{t=1}^{T} (OBS(t) - MEAN)^2} \quad (2)$$

OBS(t) is the observed value at time *t*, *SIM(t)* is the modeled value at time *t*, and *MEAN* is the mean of the full time series. ME values can range from -∞ to 1 with 0 indicating simulation results are no better than the mean, and 1 indicating perfect agreement between modeled and observed data. Negative values signify conditions where the mean is a better predictor than the model. The highest ME was obtained by applying a Manning's n of 0.017 and 0.10 for unvegetated and vegetated marsh, respectively (Table 2), similar to values determined by *French* [2003].

The modeled dye tracer was distributed over 7x10^6 particles, the maximum number of particles required to achieve the highest level of accuracy while maintaining computational stability. The accuracy of the tracer simulation was expressed as the smallest concentration that can be represented by a single particle in a computational cell. In our case, the smallest detectable concentration was 4ppb. Horizontal dispersion

parameters were set to a = 0.20m^2/s and b = 0.02, and a roughness length of 0.001m followed from model calibration. A computational time step of 0.025 minutes was used to establish numerically stable simulations, and results were output at 10-minute intervals. Dye concentrations are computed by dividing the total mass of particles in each computational cell by the cell volume.

4.3 – *Model Validation*

Visual inspection of observed vs. simulated pressure, velocity and dye concentration time series from the various stations shows that the model was largely successful in replicating the amplitude and timing for inundation and drainage. In particular, the model is highly efficient in simulating the time series at five of six stations (Figure 4). The simulated and observed data nearly overlie one another in five of the six stations and give a ME = 0.99. Station 2 has the least correspondence but maintains a robust ME = 0.92. However, the maximum and minimum water levels for each tidal cycle at Station 5 are offset by 0.10m – 0.20m, but this systematic offset appears to be a related to uncertainty in instrument position.

The ME assessment of velocity at a station was equally successful in most cases, with a range of 0.82 – 0.94 (Table 3), and the velocity asymmetry is well replicated (Figure 5). The peak flood and ebb velocities are also well represented for most stations, although Station 1 is underestimated by up to 0.20m/s at the higher stages (Figure 5). Moreover, peak flood velocities at Station 3 are consistently underestimated by 0.20m/s. Taken together the ME values indicate that the model is largely successful in its representation of stage and velocity at most stations.

Simulation results for the dye tracer at Stations 1, 2, 3, 3 grab, 5 grab, 6, 7 and 8 are overall successful in that the ME values are in the range of 0.30 – 0.83 (Table 3). Stations 1 and 2 have comparably large ME values of 0.83 – 0.82 but in both instances the peak concentrations are offset by 17ppb and 30ppb, respectively (Figure 6). The model is least efficient at Stations 3, 5 grab and 8 with ME of 0.36, 0.35 and 0.30, respectively. In these cases the overall shapes of the modeled dye responses are well-represented, but peak concentrations are offset by up to 140ppb and the timing of the modeled tracer is ~ 30 minutes earlier than observed. On the other hand, in all eight instances the offsets decrease with time (Figure 6), and more importantly all of the ME values are positive, indicating that the numerical simulations of dye movement are representative of field conditions, albeit at different levels.

4.4 – *Groves Creek Circulation*

We characterized overmarsh circulation with dye concentration data from measurements at eight stations throughout Groves Creek, and we investigated circulation over the entire Groves Creek basin by using the coupled FLOW-PART components of Delft3D to simulate the transport of a conservative tracer. The modeled dye distribution provided insight for determining the spatial scales of analysis needed to assess overmarsh circulation. We evaluated marsh circulation with maps of modeled free surface elevation, stage-velocity relationships, residence time, velocity, flux, and local currents at the fours scales of assessment.

In particular, the basin scale (1,000m) was assumed to represent spatial patterns in bulk average flows of water and dye that entered and exited the salt marsh system. Circulation at this scale was described using three approaches. First the elevation of the

free surface during the spring tide was mapped over the entire marsh at 20-minute intervals beginning at 4hrs after low water and ending 4hrs after high water. Water elevation contour maps were generated in ArcGIS and the corresponding areas of inundation were calculated for each time interval.

The second approach made use of the proximity of Station 1 to the mouth of Groves Creek. Here we assumed that the "upstream" processes that affect flow at the mouth are encapsulated in the overall shape of the velocity – stage relationship for the spring tide. In this case we plotted the field data together with the simulated data to highlight the upstream geomorphic/topographic controls on a typical entry point for water in systems such as this, and the overall ability of the simulations to represent direct measurements.

The final measure relied on tracer residence time for the 5-day interval as calculated from concentrations at stations 1, 2, 3, 6, 7 and 8. Residence time helps characterize the time required for a parcel of water to hypothetically enter and exit the system, and it can help quantify spatial variations in transport processes [*Monsen et al.*, 2002]. Assuming concentration of the tracer decreases exponentially with time and adopting equation 3 and 4 from *Miller and McPherson* [1991]

$$C(t) = C_o e^{-kt} \quad (3)$$

$$Rt = \frac{1}{k} \quad (4)$$

where *C(t)* is the concentration at time t, C_o is the initial concentration of the tracer, and k represents first order removal rate. Residence time *(Rt)* is simply the inverse of the removal rate.

Circulation was assessed at the macro scale to illustrate the spatial arrangement of velocity vectors computed over 60m x 60m grids. This grid size was selected through an iterative grid averaging process and we determined that it was the optimal grid size for the representation of macro scale flow processes. Thus, this grid size represents flows over and through the marsh interior that operate at scales on the order of about 100m. This scale was useful for shedding light on the internal circulation of the system during intermediate tidal stages as well as detecting and quantifying variations in flow paths between flood and ebb cycles. Vector maps of simulated depth averaged velocity were generated in Matlab to show circulation over a four-hour interval, two hours before and after the spring high tide.

Meso scale circulation refers to processes operating at a length scale of 10m corresponding to the flows between intertidal creeks. The meso scale approach included a flow assessment and water balance with a series of six transects across different parts of the marsh (Figure 3). Transect 1 encloses the marsh interior but was separated into two parts to account for flows between two different subtidal systems, 1a between the marsh interior and Groves Creek, and 1b between the marsh interior and the Wilmington River (Figures 1 and 3). Together transects 1a and 1b illustrate fluxes toward and away from the salt marsh interior. Therefore, net fluxes computed as the difference between inflows and outflows across these transects will reveal any overall water imbalance for the marsh interior. Transects 1a and 1b are 500m long and each consists of ten 50m long sections (Figure 3). This was advantageous for establishing transect flexibility with respect to geomorphic structure. Also, four 50m long transects (2a, 2b, 2c, and 2d) were positioned

further into the basin (Figure 3) to determine flow characteristics within the marsh interior.

For all transects the magnitude and direction of net flux were computed at 10-minute intervals and total flood and ebb fluxes were summed over their respective 390-minute intervals. The convention for describing flux direction across transects 1 and 2 is expressed as positive (+) for outflow or ebb and negative (-) for inflow or flood (Figure 3). Thus, flood and ebb volumes that do not sum to zero indicate a preferential flow direction between flood and ebb cycles. Specifically, a + volume over transect 1 indicates net flow away from the marsh interior. Likewise, consistent + values for transect 2 collectively indicate net counterclockwise flow.

Finally, micro scale circulation represents flow at a 1m scale with particular attention to the spring tide because of the fuller salt marsh inundation. In this case flow was evaluated at two locations in two intertidal creeks with a series of ~90º bends or "dogleg" bends (Figure 3). The two locations were selected to show vectors associated with the east/west and north/south sections of the dogleg. Creek 1 is a first order creek with a bank elevation of about 0.47m (Figure 3). The creek bed elevations of the north/south and east/west reaches are -0.53m and -0.38m, respectively. Creek 2 is part of an intertidal system that dissects the southern marsh interior (Figure 3). The bed elevations of the north/south and east/west sections are -0.60m and -0.66m, respectively, and the bank elevation is about 0.40m. Information on the dynamics of in-channel current direction and magnitude at these sites is useful because it can shed light on when channel structure no longer controls depth averaged flows. For example, flows with a uniform direction over a dog-leg indicate that larger scale pressure gradients dictate current

directions and magnitude, and not the creek banks. In this way, the micro scale analysis highlights local vs. basin scale controls on current complexity.

5. RESULTS

5.1 – Dye Tracer At a Station

Figure 6 shows the time series of concentrations at Stations 1, 2, 3, 3 grab, 5 grab, 6, 7 and 8 for both observed data and simulations. The field data show that the dye appears at Station 1 8hrs after release. This is consistent with the dye release "upstream" of Station 1, and on the rising tide; hence dye could not reach the station until ebb. The first peak is 45ppb and it coincides with low tide (Figure 6a). The peak duration is 20 minutes and concentrations decline to zero at high tide. Subsequent peak concentrations also coincide with low tide and decay with time. For example, successive peaks are 28ppb, 17ppb, 11ppb, 7ppb, and 4ppb, respectively, decreasing by ~ 40% with each cycle (Table 4). Also, the duration of the peaks progressively increases to 2hrs with the final tidal cycle.

The dye reaches Station 2 at the end of the ebb cycle 7.5hrs after the release, and again, because the station is "downstream" of the dye release. Peak concentrations occur at low tide and the first is 103ppb (Figure 6b) and lasts for 1.5hrs before declining to about 0 ppb at high tide. Subsequent peak values decay with time going from 52ppb, 30ppb, 18ppb, 11ppb, and 6ppb, again decreasing by ~ 40% with each cycle (Table 4). As with Station 1 the duration of the peaks increases with time and reaches a maximum of 4hrs.

Station 3 is upstream of the dye release and in the direction of transport on the rising tide. The concentration time series is more complex relative to the response at stations 1 and 2, in that it exhibits a persistent double peak that gradually diminishes over several tidal cycles (Figure 6c). The first peak occurs just after high tide on November 2nd is 130ppb and a second lower peak occurs on the rising tide. There is a local minimum that occurs between peaks at low tide and concentrations go to 0ppb at high tide. Peak concentrations decay with time going from 65ppb, 40ppb, 21ppb, 14ppb, and 8ppb (Table 4).

The observed time series at Station 3 grab reflects the 2.5-hour time interval over which grab samples were collected (Figure 6d and Appendix a). This station is also upstream of the dye release and initial concentrations reach the site about 1hr after the release. A peak concentration of 588ppb occurs just after low tide (Appendix a). Concentrations decline on the rising tide and go to zero 1.5hrs after the initial peak.

Similarly, grab samples were collected at Station 5 grab and the time series reflects the 2.5hr-sampling interval (Figure 6e and Appendix b). Station 5 grab is located upstream of the dye release in the West branch of the subtidal system. The dye plume reaches the station about 1hr after release. The largest concentration of all stations occurs as a peak of 1038ppb just after low tide (Appendix b).

Station 6 is upstream of the dye release and the response is much more complex and variable relative to the responses of other stations. The largest concentration for the time series occurs as an initial peak coinciding with the rising tide 3hrs after the dye release (Figure 6f), giving an average dye velocity of 0.16m/s. This peak goes from 0ppb to 530ppb, with the return to 0ppb occurring just before peak tide. This is followed by a

double peaked interval with successive peaks occurring at mid tide during one rise-fall interval. Concentrations decline rapidly with time and the peak duration increases from 4hrs to 8hrs (Figure 6f). Subsequent increases in concentration lack the double peak and give more of a plateau response, and successive plateau values decline at a rate of 35-40%. Another apparently consistent response in this dye time series is smaller and relatively short-lived peaks that occur just after high tide, or just before the concentrations reach the plateau values.

Station 7 is located further into the marsh interior between the subtidal system and the eastern marsh edge. The initial peak of 170ppb occurs during the first ebb tide, about six hours after the dye release (Figure 6g). Station 7 is dry at mid to low tide and this resulted in gaps of the time series. Peaks occurring during the subsequent ebb tides decrease exponentially from 89ppb, 54ppb, 38ppb, 21ppb, 16ppb, and 8ppb (Table 4).

The Station 8 data have a response similar to that of Station 1 and 2 in that they increase from zero to a consistently higher range over an interval of about four hours midway between the ebb and flood phase, and the peak values decline with each successive tidal cycle (Figure 6h). However, the data differ in that at the onset of the higher four-hour interval the concentrations attain an initial peak before declining to a quasi-steady, higher value (Figure 6h). The initial dye response occurs 7hrs after the release and peaks at 79ppb. Tracer concentrations decay exponentially with time decreasing by ~ 40% with each cycle and with 5ppb remaining after six tidal cycles (Figure 6h), and the duration of the peaks is consistently 5 hours.

In summary, peak concentrations range from 45ppb-1038ppb (Table 4), and at all sites the timing of peaks coincide with low tide. Also, concentrations go to zero at high

tide and decay exponentially between tidal cycles. Moreover, there is an initial spike in concentration at Stations 3, 3 grab, 5 grab and 6, but both Stations 1 and 2 have a single peak per tidal cycle. Hence, the stations in the ebb direction of the injection line have single peaks whereas those in the flood direction have multiple peaks.

Table 4 highlights simulated and observed peak concentrations, and the mean time series concentration for Stations 1 - 8. Overall, the table shows that the initial modeled peak concentrations are typically underestimated by 10ppb – 400ppb with the largest offset occurring at Station 5, but in all cases the differences decline with each successive tidal cycle (Table 4). By the end of the simulation most of the peak differences are less than 10ppb. The model also captures an initial peak of 150ppb at Station 3, but is completely missed by the hourly observation data (Table 4). Also, in all eight instances the mean of simulated and observed concentrations are very similar. In fact, the means are identical at Stations 1 and 6, and are only different by 1ppb – 40ppb at the other six sites, and with the largest mean differences at Stations 3 grab and 5 grab where the time series of observation data is the shortest (Table 4).

In summary, the model results mimic the observed data but there are substantial differences. Typically, the early simulation results are least representative with initial peak offsets of up to 400ppb, but they improve with time because the actual and simulated dye concentration gradients decrease with time as the plume spreads out. In addition, plotting the model results with field observations illustrates that there is an initial 30 minute offset between observation and simulations, and more importantly that this offset declines with time. Moreover, taking the mean of the time series removes phasing issues and reveals strong agreement between observed and simulated data. The

model also captures the initial peak at Station 3 that was completely missed by the observed data.

5.2 – *Dye Tracer Over the Basin*

Simulation results show that two hours after dye release (three hours before high tide) there is dye transport along Groves Creek with a faster moving core (Figure 7a). This results in a 0.40km - 0.70km long low concentration (< 50ppb) tail on either side of Groves Creek and higher concentration center plugs (> 500ppb) reaching the marsh interior through the subtidal branches (Figure 7a). For instance, high concentrations can be seen in the dissected marsh west of the Middle branch (Figure 7a, coordinates 4.976×10^5, 3.5368×10^6) and east of the middle branch (4.976, 3.5366). For brevity, we will no longer include the 10^5 and 10^6 factors when reporting coordinates. Lower concentrations are ~ 50ppb, located in Groves Creek to the south of the dye release and along the leading edges of the dye plume. Comparably high concentrations also occur in the much smaller intertidal creeks along the north side of Groves Creek, which facilitate dye transport toward the northeast and east (Figure 7a). In some cases the concentrations there exceed 500ppb and in all cases the dye is limited to the creek banks and downstream of the creek heads.

At three hours into the dye release or two hours before high tide the maximum concentrations remain about 500ppb but shifted eastward and southward (Figure 7b). This is apparent in the Middle and West branches where 500ppb concentration is located farther east relative to Figure 7a and they form a front along the marsh interior (Figure 7b). There is also a long tail of 500ppb to the west of the dissected marsh that is associated with westward transport along the southern terrestrial border (4.974, 3.5366).

There are areas of high concentration in the dissected marsh west of the middle branch that surround a central area of relatively lower concentration, indicating convergence of flow from the north, west, and east (Figure 7b). At the same time, concentrations to the west and east of the middle branch are relatively higher than in the channel, indicating flow divergence. Lower concentrations < 50ppb occur along creek networks at higher elevations centered at 4.978, 3.5372, and in the subtidal channel branches, and along the dye plume fringes (Figure 7b).

The orthorectified and color enhanced image (Figure 8) represents the conditions at 19:32 GMT or 3.5 hours after the dye release. The photo shows areas of high concentration along the southern terrestrial boundary, the dissected marsh and in the low marsh east of the subtidal system. Also, the color enhancement highlights a faint arc of low concentration on the marsh platform north of and parallel to Groves Creek. The figure also shows the absence of dye. For instance, although we injected the dye into the subtidal system 80m south of Station 2, dye is essentially undetectable in Groves Creek and in most of the length of the three subtidal branches (Figure 8). Hence, the tidal circulation forced the dye from the subtidal to the intertidal zones.

The model results at 19:00 (Figure 7b) accurately mimic the presence of high concentration in the air photo (Figure 8), as well as the presence of otherwise visually undetectable concentrations of dye, indicating that the modeled dye reached this location 30 minutes ahead of the observations. Nevertheless, figure 7b shows that the distribution of dye between subtidal and intertidal zones is comparable. Moreover, the absence of dye and areas of lower concentration in figure 7b exactly match the spatial pattern of dye free

areas recorded in the air photo. In fact, the model results enable the visualization of dye distribution of < 10ppb.

Figure 9a shows the dye simulations two hours after high tide. Concentrations are more dilute and range from 25ppb - 75ppb throughout the marsh interior and at the outer edge of the dye front. The front has a highly irregular shape with “points” that likely reflect overmarsh flow routing through intertidal creeks (Figure 9a). Also there are three areas of higher concentrations between 250ppb – 350ppb in the marsh interior (Figure 9a). One area is along the terrestrial border to the west (4.974, 3.5366). The second is to the east near the head of the major intertidal creek with Station 8, and the third occurs in the dissected marsh (4.976, 3.5368). Clearly, some dye leaves the system from the large intertidal creek along the eastern marsh edge (Figure 9a).

One hour later (three hours after high tide) the simulations show dye retention in the marsh but with limited extent, mainly confined to the south (Figure 9b). The ebb concentrations are much lower relative to Figure 9a, typically in the range of 25ppb – 60ppb with two areas of higher concentration of up to 150ppb in the southwest (4.972, 3.5367) and southeast (4.9808, 3.5369). The dye plume extends downstream of the injection point, and some trace amounts of dye leave the system through the mouth of Groves Creek while much more concentrated dye leaves through the major intertidal creek to the east (Figure 9b). The irregular-shaped and dilute dye front on the marsh platform to the north has an apparent uniform shape between figures, indicating that water at the heads of creeks does not flow through the intertidal creek system, but across them before entering Groves Creek (Figure 9b). The major intertidal system to the east is clearly an important part of salt marsh drainage as indicated by the higher concentrations

feeding into it. In fact, we determined that 12% of the total dye mass exited the system from the eastern marsh edge, while 7% exited via the mouth of the main channel over the first full tidal cycle. Moreover, over the full five-day simulation interval we found that 53% of the total dye mass exited the system from the eastern marsh edge while 32% exited via the mouth of the Groves Creek. The remaining 15% was retained in the marsh interior.

In summary, the modeled dye transport results highlight the complexity in inundation timing and flow direction throughout the basin, and patterns of overmarsh circulation. The tracer reveals that the interior dissected marsh area first inundates from the east through the Middle branch, and subsequently from the west through the relatively longer West branch. Moreover, there is simultaneous flow divergence and convergence in the marsh interior. Also, the dye results show differences between flood and ebb circulation indicating that water parcels on the flood do not necessarily follow a similar but reversed path on ebb. Finally, after six tidal cycles most of the dye was transported out of the system via the eastern marsh edge.

5.3 – *Basin Scale Circulation*

Figure 10 shows contours of the simulated free surface elevation during spring tide inundation. At 8:40 46% of the area is inundated and the water surface elevation is < 0.67m (Figure 10a). During this time water is confined to the subtidal system, some lower intertidal creek networks, and low marsh. Just 20 minutes later 72% is inundated including lower areas of the marsh platform; while the higher areas and levees are dry (Figure 10b). The free surface elevation is 0.76m along the eastern marsh edge, 0.71m in the subtidal channel and intertidal creeks, and <0.67m in the marsh interior. At 9:20 91%

of the marsh is submerged, with mostly levees being subaerial (Figure 10c). The maximum water surface elevation is 0.87m along the eastern marsh edge and 0.79m in the marsh interior. At 9:40 98% of the marsh is inundated and only the highest levees along the main channel are dry (figure 10d). The water surface is 1.03m along the eastern marsh edge, 0.98m in the marsh interior, and 0.95m in the southwest. The distance between minimum and maximum elevations is 500m yielding a maximum slope of 1.6×10^{-4} toward the southwest and indicating inundation from the basin exterior and to a lesser extent intertidal creeks and Groves Creek. At 10:00 99% of the marsh is inundated and only the two highest levees along the first and third bend in Groves Creek are subaerial (Figure 10e). The elevation of the water surface is 1.15m along the eastern marsh edge and decreases to 1.11m in the west and the maximum slope toward the southwest decreases to 8×10^{-5}. At this time the source of water inundating the marsh is from the basin exterior, rather than from subtidal and intertidal conduits. At 10:20 the entire marsh is inundated and the free surface elevation is > 1.25m. The two highest levees remain submerged over the final 20 minutes (Figure 10f).

Model results also show in-channel variations in surface water topography. At 9:00 there is a 0.03m higher water level along the outside bank of the second bend in the channel. More importantly, the same phenomenon occurs at bends along Groves Creek, far from the domain boundaries. This accumulation of water in channel bends has been reported by [*Georgas and Blumberg*, 2003, and others] and it corresponds to the effects of centrifugal acceleration.

System drainage is illustrated by Figure 11. At 12:00 the entire marsh is submerged starting with a bulge of water of 1.25m focused in the southwest part of the

basin (Figure 11a). The elevation decreases outward to 1.19m indicating radial drainage toward the basin's eastern perimeter. At 12:20 (Figure 11b) the two highest levees along the first and third bends of Groves Creek reemerge. The water elevation decreased 0.15m in 20 minutes, and the free surface elevations range from 1.11m in the marsh interior to 1.02m in the north and along the eastern marsh edge. The distance between the minimum and maximum elevations is 500m yielding a slope of 1.8×10^{-4} toward the east capable of forcing a strong flow over the eastern marsh edge. At 12:40 all levees along Groves Creek become emergent (Figure 11c), and the maximum elevation is 0.99m in the marsh interior and 0.87m in the north and eastern marsh edges, yielding an increased maximum slope of 2.4×10^{-4} toward the east and increased flow over the marsh edge. At 13:00 the elevation decreases from 0.85m in the marsh interior to 0.67m in the subtidal channel and high intertidal creeks. The eastward slope between the marsh interior and the eastern marsh edge increases to 3.6×10^{-4}. At 13:20 24% of the marsh is subaerial, including levees, high areas of marsh platform, and intertidal creeks. The water surface elevation is 0.72m across the western low marsh and in the marsh interior (Figure 11e) and < 0.67m in the subtidal channel, intertidal creeks, and to the west and east of the marsh interior. At this time the basin drains toward the west and east of the marsh interior through intertidal creeks and Groves Creek. At 13:40 53% of the marsh is subaerial and the free surface is < 0.67m (Figure 11f).

In summary, the free surface slopes, and hence the direction of inundation changes as the percentage of inundated area increases. Inundation occurs from the interior by flow from the subtidal to intertidal creeks during the first four hours when 46% of the basin is inundated. Between 9:00 and 9:40 inundation increases, the relief of

the water surface increases to 0.08m and the resulting slope increases to $1.6x10^{-4}$; also the eastern marsh edge, intertidal creeks and the subtidal channels are submerged at this time. Two hours before high tide the entire marsh is submerged, the maximum difference in water surface elevation is 0.04m, maximum slope decreases to $8x10^{-5}$, and there is a change in the source of inundation going from the subtidal system to overmarsh flow toward the southwest. Similarly, ebb circulation changes with decreasing area of submergence. At the onset of drainage water leaves the salt marsh as a type of sheetflow outward from the southwest toward the basin perimeter, and it persists for the first 3 hours of ebb. An hour later the marsh topography becomes subaerial, and there is a maximum slope of $1.8x10^{-4}$ to the east indicating strong flow over the eastern marsh edge, followed by flow divergence in the marsh interior.

Another insightful way to assess basin scale flow is to evaluate the stage-velocity association at a station, in this case near the mouth of Groves Creek, Station 1 (Figure 12). The observations show that the peak flood and ebb velocities are comparable and have the characteristic asymmetry with ebb dominance [*Myrick and Leopold*, 1963; *Boon*, 1975; *Pethick*, 1980; *French and Stoddart*, 1992; *Fagherazzi et al*., 2008]. In particular, peak flood velocity occurs at a higher stage than peak ebb. For example, on the spring tide the peak occurs at 1.15m and peak ebb occurs at 0.40m (Figure 12). Meanwhile velocity reaches 0.51m/s between a low tide elevation range of -1.68m - 0.63m. Subsequently, there is a surge in velocity reaching a peak of 0.93m/s at 1.15m (Figure 12). Currents then reverse and peak ebb velocity of -0.95m/s occurs at 0.7m.

The modeled stage-velocity relationship is comparable. Overall it shows flood velocity increases to 0.52m/s between a low tide range of -1.67m - 0.62m (Figure 12).

This is followed by a surge in velocity reaching a peak of 0.69m/s at 0.93m. Currents reverse and peak ebb of -0.95m/s occurs at 0.35m. Velocities then decrease between peak and low tide and much more rapidly than during flood. Comparing the observed and simulated data shows that the model accurately predicts the overall stage-velocity relationship for Station 1.

Both the simulated and observed datasets show ebb velocities decreasing at a faster rate than during the same stages of flood. Moreover, the model captures the surge in flood velocity at stages when the topography is submerged and overmarsh flow is initiated [*Boon*, 1975; *French and Stoddart*, 1992]. Both curves also show comparable asymmetry between peak flood and ebb velocity during higher stages. Specifically, peak flood is tied to the marsh platform elevation, as expected. Together these observations and analyses show that the modeled and observed flows at the mouth of the main channel are comparable, and the "upstream" overmarsh flow processes that give rise to the velocity-stage shape and distributions are also comparable, as well.

A third metric for assessing basin scale flow makes use of residence time, an estimate of the duration of a water parcel in the basin system. The tracer residence time (Rt) expressed through equation 3 and calculated from the observation data at Stations 1, 2, 3, 6, 7 and 8 ranges from 1.09 – 1.12 days with an average of 1.07 days (Table 5). The modeled Rt values are comparable, ranging from 1.02-1.12 days (Table 5). Therefore, we can expect that the innermost water parcels will be flushed from the system within about 1 day.

5.4 – *Macro Scale Circulation*

At two hours before high tide the mean depth of water on the marsh platform is 0.58m. The mean velocity over the platform and eastern marsh edge is 0.02m/s and 0.08m/s, respectively (Figure 13a). The average flow vectors along the eastern marsh edge and in the north (Figure 13a coordinates 4.980, 3.5372) indicate inundation predominantly from the basin edges as opposed to the channel network. However, in the southern marsh interior centered at approximately (4.977, 3.5366) there is divergent flow toward the west and east along the southern boundary (Figure 13a). Also, there is clockwise flow centered at 4.981, 3.5368 over the marsh interior with an average speed of 0.05m/s; decreasing to 0.03m/s along the central marsh interior where east - west convergence occurs. Hence, during flood and over the relatively short distances associated with this basin we find that overmarsh circulation concomitantly includes convergence and divergence in the marsh interior, and primarily convergence from the basin perimeter.

Figure 13b sheds light on local flow two hours after high tide. The mean velocity over the marsh platform and eastern marsh edge is 0.04m/s and 0.11m/s, respectively, and both show three circulation patterns during ebb. First, there is counterclockwise flow (Figure 13b) centered at (4.981, 3.537) that extends from the southwest across the marsh interior at 0.08m/s (Figure 13b). Second, there is flow divergence from the marsh interior toward the west and east of the counterclockwise flow path. Third, there is flow toward the basin exterior north of the marsh platform (4.980, 3.5374), and over the eastern marsh edge. Hence, the flows during ebb show similar complexity as with flood, with a range of flow directions over a relatively short time interval.

In summary, during flood, three distinct circulation patterns occur simultaneously. First, there is inundation toward the southwest from the basin exterior. Second, there is clockwise flow over the marsh interior. Third, there is flow divergence toward the east and west along the southern extremities of the basin, and flow convergence in the marsh interior. Ebb circulation differs from flood in that ebb velocities are stronger relative to flood. Also, flow across the marsh interior is counterclockwise, and there is flow divergence to the east and west of the marsh interior.

5.5 – *Meso Scale Circulation*

The meso scale results from transects 1a and 1b are presented as a water balance across each. These two transects were used because basin scale analyses revealed that there are two sources of water to the marsh interior; Groves Creek and the Wilmington River. The net volume of water that crosses transect 1a during flood is -3,452m^3 while for ebb it is +8,498m^3 (Table 6). Therefore, the difference between flood and ebb is +5,046m^3 over the full tidal cycle. Flood and ebb volumes across transect 1b are -3,700m^3 and +11,720m^3, respectively, with net volume of +8,020m^3. Both have positive net transport over the full tidal cycle indicating net flow away from the marsh interior.

Meanwhile, information gleaned from the net flows across transects 2a-2d are taken to represent flows within the marsh interior. Water volumes range from -2,459m^3 to -16,080m^3 for flood and +4,280m^3 to +28,428m^3 for ebb (Table 6). The differences between flood and ebb range from +1,741m^3 to +22,407m^3. All four transects have positive net transport over the full tidal cycle and collectively they indicate net counterclockwise or rotational flow within the marsh interior.

5.6 – *Groves Creek Circulation – Micro Scale*

At the micro scale we assess the current velocity time series for two intertidal creeks with a dogleg structure (Figure 3) to illustrate the local control of topography on overmarsh circulation. Creek 1 is inundated from the south at 3 hours into the flood cycle (Figure 14a). Currents are confined to the channel and both locations reach a peak flood velocity of 0.09m/s. At approximately 0.67hrs later the water level is 0.53m and currents in both sections flow from the northwest, and velocity is 0.06m/s lower. The consistent southeastward flow through both sections of the dog-leg indicates the onset of overmarsh flow which continues at 0.02m/s until high tide (1.45m).

At the start of ebb the water level is 1.44m and the depth averaged currents in both the north/south and east/west sections are from the west at 0.04m/s (Figure 14a). One hour into ebb the water level declines to 1.28m and overmarsh currents reverse reaching a peak of 0.26m/s. Four hours after high tide the water level is at 0.45m and the creek banks become subaerial. At this time the in-channel currents reverse and flow from the north-northeast at 0.09m/s.

Creek 2 is inundated 2hrs into flood when the water level is -0.42m and currents are confined by the banks. At the same time there is convergence from the subtidal channel and eastern marsh interior (Figure 14b). At 0.33hrs later in-channel currents reverse and flow from the north occurs when the water level reaches -0.14m, and develops a peak velocity of 0.20m/s. Four hours into flood the topography is submerged and at that time overmarsh currents flow from the northeast at 0.03m/s until high tide (Figure 14b).

With the onset of ebb, overmarsh flow is from the southeast at 0.04m/s (Figure 14b). The topography becomes subaerial three hours into ebb at a water level of 0.69m.

At this time in-channel currents reverse and reach a peak velocity of 0.23m/s. Four hours into ebb there is another current reversal at -0.27m, and flow is from the northwest at 0.07m/s.

In summary, Creek 1 activates three hours into the flood tide and creek banks are submerged less than an hour later. During ebb this creek is active for 2 hours. Creek 2 has a relatively lower bed elevation than Creek 1, activates at two hours into flood, and is submerged 2 hours longer, but it reactivates during the last 3 hours of the ebb tide. The velocity and direction of in-channel and overmarsh currents supports the reported observations for meso, macro, and basin scale results by collectively showing clockwise and counterclockwise patterns of overmarsh flow during flood and ebb, respectively.

6. DISCUSSION

We define complexity in overmarsh circulation as the variation in current direction and magnitude over relatively short time intervals of about 10 minutes. Flow complexity has been a common theme in salt marsh flow studies [*Eiser and Kjerfve,* 1986; *Kjerfve,* 1991; *Christiansen et al.,* 2000; *Temmerman et al.*, 2005; *Torres and Styles*, 2007; *Mariotti and Fagherazzi*, 2011]; yet no studies have characterized this complexity for a comparably large section of salt marsh as conducted here, and none have addressed its origin. Here we found that the source for the onset of complex overmarsh circulation is the submergence and emergence of the very subtle salt marsh platform relief. For example, emergent topography can completely shut off some flow pathways while initiating new ones.

The spatial variability in dye concentration from the model largely replicates field observations as indicated by the strongly positive ME values. Results were somewhat less robust at Stations 3, 5 and 8. We propose that the Station 3 (ME = 0.36) discordance arose because the simulations produced a large initial spike in concentration that was not detected in the hourly observation data. Given equation 2 this translates directly to a poor model performance. The lower ME for Station 5 likely is a product of the phase offset between simulation and observation over the full two hour record for these grad samples. However, phase shifts are also apparent with all comparisons of simulated and observed but the shift declines over the 5-day interval. Therefore, given the short record of comparison and the exclusion of the latter data for comparison the Station 5 ME value reflects substantial discordance. At Station 8, the only station in the intertidal zone and the one most distant from the injection line has a weak performance that is also attributable to phasing. In this case the observed initial spike increase in concentration occurs earlier than the simulated. This may have arisen due to the longer and hydrodynamically rougher intertidal zone distance that water must traverse to reach the station. Despite these limited shortcomings, the dye response at all stations was well represented by the model, and provides reliable background flow information on system wide inundation and drainage.

Residence time, Rt gives an estimate of the duration of a water parcel in the basin system, and the simulation results show that Rt is about 1.11 days. This residence time is 28% greater than the basin flushing time, Tf, most likely because of the spatial and temporal variability of underlying physical processes controlling overmarsh circulation.. Additionally, *Blanton et al.*, [2010] measured concentrations from a site proximal to

Station 2, and they estimated Rt of 1.62 days. Therefore, our values are about 0.5 days shorter, and they further constrain plausible estimates of Rt in salt marsh systems.

Dye circulation patterns reveal that the sheet flow over the largely flat salt marsh landscape is not homogeneous, but has strong temporal and spatial variability that arise from simultaneous convergence, divergence and rotation in the marsh interior during flood. This type of complexity in overmarsh circulation is important in salt marshes because it strongly influences the distribution of suspended and dissolved nutrients, larvae distribution, and contaminant dispersal [*Valiela et al*., 1978; *Kneib*, 1984; *Blanton et al.*, 2010]. For instance, the flow fields in Figures 13a and 13b illustrate the source of the dye front that occurs 2hrs before high tide. The dye circulation also shows that there is considerable drainage directly over the eastern marsh edge during ebb. Hence, a parcel of inundation water does not necessarily follow the same track between flood and ebb [e.g., *French and Stoddart*, 1992]. The dye response also highlights spatial variability in flow complexity throughout the Groves Creek system. For instance, stations located in the ebb direction of the injection have single peaks coincident with low tide, whereas all other stations have double peaks, one on the ebb and one on the flood limbs of tidal stage. A similar response in salinity was reported by Warner et al. [2006] who attributed the double peak to confluence effect at tributary channels [*Warner et al.*, 2006]. On the other hand Station 8 has a double peak as well, but for entirely different reasons. The difference resides with the fact that Station 8 is intertidal zone. Here the double peak is a result of the intermittent drying of the creek bed with low tide and the movement of the dye tracer back and forth over the site with each tidal cycle. Taken together, the dye

response and underlying flow conditions highlight overmarsh flow complexity across relatively large distance and at a range of spatial scales.

Analyses at the four spatial scales of flow highlight patterns of overmarsh current direction, and two of the four highlight both direction and magnitude. At the basin scale we saw that the direction of inundation and drainage changes over short time intervals and this, in turn, is related to the degree that the marsh remains subaerial. At the macro scale, we show flow direction and magnitude for intermediate tidal stages. The data analyses clearly show that there is simultaneous convergence and divergence, as well as rotational flow and substantial flow over the marsh edge.

At the meso scale flows across transect 1 indicate that net transport is away from the marsh interior, and ebb dominant. The variability between 1a and 1b may be set by the average transect elevation with 1a at 0.62m ±0.09m, and 1b at 0.56m ±0.15m. Also, these transects essentially represent water exchange between the marsh interior and Groves Creek, and the marsh interior and the Wilmington River, 1a and 1b, respectively. Therefore, we contend that the net fluxes reflect a type of circulation where water inundates the marsh through the channel network but principally drains over the marsh edge. This is consistent with the tracer and macro scale flow results. We also show positive net flow for transects 2a-2d and this is taken with their respective spatial arrangement to indicate counterclockwise rotation during part of the tidal cycle [Figure 3, Table 6].

At the micro scale we show that intertidal creeks are active only during a small portion of the tidal cycle, and for about one hour longer during ebb tide than flood. The time that intertidal creeks convey flow is of course dependant on bed elevation, and these

vary substantially. The intermittent control of topography on local in channel currents together with shifts in the larger scale barotropic pressure gradient give rise to additional current reversals during flood and ebb [e.g. *Torres and Styles*, 2007; *Fagherazzi et al.*, 2008]. Clearly, topography is an important control on overmarsh circulation. In a recent study, *Blanton et al.* [2010] conducted numerical simulations over the same study site, Groves Creek, but they used a bathymetric domain derived from a coarse lidar dataset. This means that their study did not include the effects of relatively small scale variations in topography or geomorphic structure. Overall, their current simulation results were fairly robust but their simulated dye plume failed to match the field observations in that the dye did not reach the southern basin edge. Also, the dye was retained in the marsh interior for a prolonged interval. Here we improve on this effort by resolving the subtle geomorphic structure and evaluating its effects on flow. Overall, the dye reached deeper into the system but our estimates for tracer residence time were much shorter than *Blanton et al*. Our findings lead us to question the level of topographic detail needed to adequately replicate overmarsh flow processes. Finally, future work is needed to address the combined role of topography and vegetation drag on the temporal and spatial variability in overmarsh circulation and morphodynamics.

7. CONCLUSIONS

The simulation results from Delft3D are robust and in most cases produced a model efficiency greater than 0.90. This is primarily due to the extremely high quality salt marsh DEM and the range and quality of field data for calibration and validation. Numerical assessments of dye transport and circulation reveal strong complexity in

overmarsh currents with the temporal evolution of inundation, and drainage at water levels within 0.2m of the mean platform elevation. Moreover, over the full five-day simulation interval we found that 53% of the dye mass exited the system at the eastern marsh edge, while 32% exited via the mouth of Groves Creek. At the basin scale (1,000m) the marsh platform is initially inundated from the marsh interior but as the tide continues to rise flooding occurs from the basin edges, and this gives rise to the onset of overmarsh flow. At the macro scale (100m) flow paths are highly variable with strong differences between ebb and flood circulation. At the meso scale (10m) we detected rotational flow over the marsh interior and across channels. At the micro scale (1m) local in-channel currents are intermittently controlled by the channel banks but at higher tide stages the larger scale barotropic pressure gradient causes the currents to flow across tidal creek networks.

ACKNOWLEDGEMENTS:

We gratefully acknowledge the following agencies for supporting this research: U.S. DOE Grant # DE-AC09-96SR1850, and PADI Research Foundation Grant # 10911. We also thank Paul Pope and Los Alamos National Lab for providing orthorectified aerial imagery, and Dr. Richard Viso and Coastal Carolina University for the multibeam survey. All data reported in this paper can be made accessible through the authors.

REFERENCES:

Abdelrhman M.A. (2005), Simplified modeling of flushing and residence times in 42 embayments in New England, USA, with special attention to Greenwich Bay, Rhode Island, *Estuar. Coast. Shelf S.,* 62, 339-351, doi:10.1016/j.ecss.2004.09.021.

Allen J.R.L. (2000), Morphodynamics of holocene salt marshes: a review sketch from the Atlantic and southern North Sea coasts of Europe, *Quart. Sci. Rev.,* 19, 1155-1231.

Blanton J.O., A.J. Garrett, J.S. Bollinger, D.W. Hayes, L.D. Koffman, J. Amft, and T. Morre (2010), Transport and retention of a conservative tracer in an isolated creek-marsh system, *Estuar. Coast. Shelf S.,* 87, 333-345, doi:10.1016/j.ecss.2010.01.010.

Boon J.D. (1975), Tidal discharge asymmetry in a salt marsh drainage system. *Limnol. Oceanogr.,* 20(1), 71-80, doi:10.4319/lo.1975.20.1.0071.

Bouma T.J., L.A. van Duren, S. Temmerman, T. Claverie, A. Balanco-Garcia, T. Ysebaert, P.M.J. Herman (2007), Spatial flow and sedimentation patterns within patches of epibenthic structures: Combining field, flume and modeling experiments, *Cont. Shelf Res.*, 27(8), 1020-1045, doi:10.1016/1.csr.2005.12.019.

Cea L. and J.R. French (2012), Bathymetric error estimation for the calibration and validation of estuarine hydrodynamic models, *Estuar. Coast. Shelf S.*, 100, 124-132, doi:10.1016/j.ecss.2012.01.004.

Chen S. and R. Torres (2012), Effects of geomorphology on the distribution of metal abundance in salt marsh sediment, *Estuaries and Coasts*, 35, 1018-1027, doi:10.1007/s12237-012-9494-y.

Christiansen T., P.L. Wiberg and T.G. Milligan (2000), Flow and sediment transport on a tidal salt marsh, *Estuar. Coast. Shelf S.*, 50, 315-331, doi:10.1006/ecss.2000.0548.

Csanady G.T. (Ed) (1973), Turbulent diffusion in the environment (No. 3), Springer.

Dyer K.R. (1973), Estuaries: a physical introduction, *Wiley Interscience*. New York.

Eiser W.C. and B. Kjerve (1986), Marsh topography and hypsometric characterisics of a South Carolina salt marsh basin, *Estuar. Coast. Mar. Sci*., 23, 331-345.

Fagherazzi S., G. Mariotti, A.T. Banks, E.J. Morgan and R.W. Fulweiler (2014), The relationships among hydrodynamics, sediment distribution, and chlorophyll in a mesotidal estuary. *Estuar. Coast. Shelf S.*, 144(1), 54-64.

Fagherazzi S., M. Hannion, and P. D'Odorico (2008), Geomorphic structure of tidal hydrodynamics in salt marsh creeks, *Water Resour. Res.,* 44(2), doi: 10.1029/2007WR006289.

French J.R. (2003), Airborne lidar in support of geomorphological and hydraulic modeling, *Earth Surf. Process. Land.*, 28, 321-335, doi:10.1002/esp.484.

French J.R. and D.R. Stoddart (1992), Hydrodynamics of salt marsh creek systems: implications for marsh morphological development and material exchange, *Earth Surf. Process. Land.,* 17, 2335-252.

Georgas N. and A. F. Blumberg (2004), The influence of centrifugal and Coriolis forces on the circulation in a curving estuary, *Estuarine and Coastal Modeling, ASCE*, 541-558.

Kjerfve, B., L.B. Miranda and E. Wolanski (1991), Modelling water circulation in an estuary and intertidal salt marsh system, *Neth. J. Sea Res*., 28(3), 141-147.

Kneib R. T. (1984), Patterns of invertebrate distribution and abundance in the intertidal salt marsh: causes and questions. *Estuaries*, *7*(4), 392-412.

Kostka J.E., B. Gribsholt, E. Petrie, D. Dalton, H. Skelton and E. Kristensen (2002), The rates and pathways of carbon oxidation in bioturbated saltmarsh sediments, *Limnol. Oceanogr,* 47(1), 230-240.

Lawrence D.S.L., J.R.L. Allen and G.M. Havelock (2004), Salt marsh morphodynamics: an investigation of tidal flows and marsh channel equilibrium. *J. Coastal Res.,* 20(1), 301-316, doi:10.2112/1551-5036.

Leonard L.A. (1997), Controls of sediment transport and deposition in an incised mainland marsh basin, Southeastern North Carolina, *Wetlands*, 17(2), 263-274.

Leonard L.A. and D.J. Reed (2002), Hydrodynamics and sediment transport through tidal marsh canopies, *J. Coastal Res*., 36, 459-469.

Leonard L.A. and M.E. Luther (1995), Flow hydrodynamics in tidal marsh canopies, *Limnol. Oceanogr*., 40(8), 1474-1484.

Leopold L.B., J.N. Collins and L.M. Collins (1993), Hydrology of some tidal channels in estuarine marshland near San Francisco, *Catena*, 20(5), 469-493.

Lesser G.R. (2000), Computation of three-dimensional suspended sediment transport within the Delft3D-FLOW module, *M.S. thesis*, UNESCO-IHE Institute for Water Education, Delft, The Netherlands.

Lesser G.R., J.A. Roelvink, J.A.T.M. Van Kester and G.S. Stelling (2004). Development and validation of a three-dimensional morphological model, *Coast. Eng.*, 51(8), 883-915.

Loder N.M., J.L. Irish, M.A. Cialone and T.V. Wamsley (2009), Sensitivity of hurricane surge to morphological parameters of coastal wetlands, *Estuar. Coast. Shelf S.,* 84(4), 625-636.

Marciano R., Z.B. Wang, A. Hibma and H.J. de Vriend (2005), Modeling of channel patterns in short tidal basins, *J. Geophys. Res.*, 110, F01001, doi:10.1029/2003JF0000092.

Mariotti G. and S. Fagherazzi (2011), Asymmetric fluxes of water and sediments in a mesotidal mudflat channel, *Cont. Shelf Res.*, 31(1), 23-36.

McKean J., D. Tonia, C. Bohn and C.W. Wright (2014), Effects of bathymetric lidar errors on flow properties predicted with a multi-dimensional hydraulic model. *J. Geophys. Res.,* 119, 644-664, doi:10.1002/2013JF002897.

Miller R.L. and B. F. McPherson (1991), Estimating estuarine flushing and residence times in Charlotte Harbor, Florida via salt balance and a box model, *Limnol. Oceanogr*., 36(3), 602-612, doi:10.4319/lo.1991.36.3.0602.

Monsen N.E., J.E. Cloern and L.V. Lucas (2002), A comment on the use of flushing time, residence time, and age as transport time scales, *Limnol. Oceanogr*., 47(5), 1545 – 1553.

Myrick R. M. and L.B. Leopold (1963), *Hydraulic geometry of a small tidal estuary*, 12-18, Washington, DC: US Government Printing Office.

Nash J. and J.V. Sutcliffe (1970), River flow forecasting through conceptual models part I—A discussion of principles, *J. Hydrol*., 10(3), 282-290.

Nixon S.W. (1980), Between coastal marshes and coastal waters – a review of twenty years of speculation and research on the role of salt marshes in estuarine productivity and water chemistry, *Estuarine and Wetland Processes Marine Science*, 11, 437-525.

Pethick J.S. (1980), Velocity surges and asymmetry in tidal channels, *Estuarine and Coastal Marine Science*, 11(3), 331-345.

Shih S.F. and G.S. Rahi (1982), Seasonal variations of Manning's roughness coefficient in a subtropical marsh, *Trans. Am. Soc. Agric. Eng.*, 25(1), 116-119.

Temmerman S., T.J. Bouma, G. Govers, Z.B. Wang, M.B. de Vries and P.M.J Herman (2005), Impact of vegetation on flow routing and sedimentation patterns: three dimensional modelling for a tidal marsh. *J. Geophys Res*., 110.

Torres R. and R. Styles (2007), Effects of topographic structure on salt marsh currents, *J. Geophys Res*., 112, F02023, doi:10.1029/2006JF000508.

Tsihrintzis V. and E.E. Madiedo (2000), Hydraulic resistance determination in marsh wetlands, *Water Resour. Res.*, 14(4), 285-309.

Valiela I., J.M., Teal, S. Volkmann, D. Shafer and E.J. Carpenter (1978), Nutrient and particulate fluxes in a salt marsh ecosystem: tidal, *Limnol. Oceanogr.*, 23(4), 798-812.

Warner J.C., D.H. Schoellhamer, J.R. Barau and S.G. Scholadow (2006), Flow convergence caused by a salinity minimum in a tidal channel, *San Franc. Estuary Watershed Sci.*, 4(3), 91-102.

Wilson C.A.M.E. and M.S. Horritt (2002), Measuring the flow resistance of submerged grass, *Hydrol. Process.*, 16(13), 2589-2598.

Table 1: List of instruments at the eight observation stations.

Station	Instrument Type
1	ADCP, SBE16 CTD, Wetlabs FLRHSB
2	ADCP, Wetlabs FLRHSB
3	ADCP, SBE16 CTD, Wetlabs FLRHSB, grab samples
4	ADCP
5	ADCP, grab samples
6	ADCP, Wetlabs FLRHSB
7	ISCO sampler, SBE16 CTD
8	SBE16 CTD, Wetlabs FLRHSB

Table 2: A list of literature sources for Manning's roughness coefficients for vegetated and unvegetated marsh[1].

Author	**Study Site Type**	**Manning's n**
Shih and Rahi [1982]	Subtropical marsh	0.16 – 0.55
Kierfve et al., [1991]	Vegetated marsh	0.20 – 0.30
Leopold et al., [1993]	Marsh channel	0.28 – 0.063
Tsihrinitzis and Madiedo [2000]	Vegetated marsh	0.02 – 1.00
Wilson and Horritt [2002]	Submerged vegetation	0.05
	Unsubmerged vegetation	0.23
French [2003]	Subtidal channel	*0.017
	Intertidal channel	0.022
	Tidal flat	0.035
	Marsh platform	*0.10
Lawrence et al., [2004]	Marsh platform	0.07
	Moderately rough channel	0.03
Lesser et al., [2004]	Uniform marsh	0.028
Temmerman [2005]	Marsh bottom roughness	0.006
Loder et al., [2009]	Sea bed	0.02
	Marsh creek bed	0.02
	Platform with tall grass	0.035
Cea and French [2012]	Subtidal channel	0.02
	Low intertidal marsh	0.03
	High intertidal marsh	0.05

[1]Citations with an asterisk were final selections for the study.

Table 3: Model efficiency values for water level, velocity, and dye tracer concentrations.

	Water Level ME	**Velocity ME**	**Dye Tracer ME**
Station 1	0.99	0.92	0.83
Station 2	0.99	0.92	0.82
Station 3	0.99	0.82	0.36
Station 3 grab	n/a	n/a	0.62
Station 4	0.99	0.86	n/a
Station 5	0.92	0.94	0.35
Station 6	0.99	0.85	0.58
Station 7	n/a	n/a	0.76
Station 8	n/a	n/a	0.30

Table 4: Observed and simulated peak concentrations in ppb, record mean and standard deviation for Station 1-8[1].

	Station 1	Station 2	Station 3	Station 3 grab	Station 5 grab	Station 6	Station 7	Station 8
Peak 1 OBS	45	103	13	588	1038	574	170	79
Peak 1 SIM	37	76	150	489	674	495	155	50
Peak 2 OBS	28	52	130	n/a	n/a	119	89	57
Peak 2 SIM	23	41	63	43	55	90	125	90
Peak 3 OBS	17	30	65	n/a	n/a	55	54	34
Peak 3 SIM	16	25	32	23	33	48	68	89
Peak 4 OBS	11	18	40	n/a	n/a	34	38	17
Peak 4 SIM	10	17	20	14	20	40	40	42
Peak 5 OBS	7	11	21	n/a	n/a	18	21	12
Peak 5 SIM	6	10	13	8	13	25	23	19
Peak 6 OBS	4	6	14	n/a	n/a	12	16	5
Peak 6 SIM	4	6	8	6	8	12	11	16
Peak 7 OBS	n/a	n/a	8	n/a	n/a	6	8	n/a
Peak 7 SIM	n/a	n/a	5	4	4	6	9	n/a
Record Mean OBS	5	15	22	85*	168*	27	41	13
Record Mean SIM	5	13	12	124*	183*	27	28	14
Record STDV OBS	10	25	28	165*	304*	45	37	21
Record STDV SIM	9	19	16	145*	196*	46	30	17

[1]Asterisks denote values calculated for a single tidal cycle at grab sample locations.

995 Table 5: Tracer residence time in days for Stations 1, 2, 3, 3 grab, 5 grab, 6, 7 and 8.

	Station 1 (Rt)	**Station 2 (Rt)**	**Station 3 (Rt)**	**Station 3 grab (Rt)**	**Station 5 grab (Rt)**	**Station 6 (Rt)**	**Station 7 (Rt)**	**Station 8 (Rt)**
Observed	1.12	1.09	0.97	n/a	n/a	1.04	1.09	1.09
Simulated	1.18	1.2	1.07	1.14	1.14	1.08	1.02	1.12

996

Table 6: Net volume transport resulting from the meso scale analysis from transects 1a and 1b, and 2a, 2b, 2c and 2d[1].

Transect	**Net Flood m^3**	**Net Ebb m^3**	**Net Volume m^3**
1a	-3452	+8498	+5,046
1b	-3700	+11720	+8,020
2a	-2539	+4280	+1,741
2b	-16080	+28428	+12,348
2c	-8146	+20666	+12,520
2d	-2459	+24866	+22,407

[1] The positive and negative values associated with 1a and 1b represent flow away from and toward the salt marsh interior, respectively. Positives and negatives associated with 2a-2d collectively represent counterclockwise and clockwise circulation within the marsh interior.

FIGURE CAPTIONS:

Figure 1: Groves Creek is a semi-enclosed creek-marsh system located approximately 20 km south of Savannah GA, USA. The shading of the imagery reflects variations in vegetation density. Specifically, lighter shades in the dissected marsh and along creek heads are associated with unvegetated mud. Darker shades along levees and creek banks reflect areas of dense vegetation. Medium shades are associated with the vegetated marsh platform. The lighter shading of the marsh platform in the northeast is associated with an area of sparsely vegetated high marsh. Groves Creek has three subtidal branches labeled E, W and M for East, West and Middle, respectively. The white dashed line outlines the "marsh interior". Within the marsh interior is the "dissected marsh" which is bounded by the West and East subtidal branches.

Figure 2: Tidal oscillations for a two week period showing the transition from neap to spring tide. The black box marks the 5-day study period. The smallest and largest tidal ranges during the study period are highlighted with gray and striped boxes, respectively, and are referred to as "neap" and "spring". All water levels are referenced to NAVD88.

Figure 3: The high resolution GPS DEM is shown. White to black on the color bar represents the elevation range associated with levee, marsh platform, low marsh, intertidal creeks, and subtidal channel, respectively. White circles mark the locations of pressure sensors, ADCPs, fluorometers, and grab samples. The small gray line south of Station 2 marks the location of the dye release. The white lines throughout the marsh interior represent the six transects used to estimate meso scale flux. Transects lengths are 500m for 1a and 1b and 50m for 2a, 2b, 2c, and 2d. The + and - illustrate the flow convention for the meso scale analysis. For transects 1a and 1b, positive flows represent net transport away from the marsh interior. For transects 2a-2d, positive flows represent net counterclockwise flow within the marsh interior. Finally, the locations of dogleg creeks 1 and 2 selected for the micro scale assessment are highlighted with black boxes.

Figure 4: The calibrated water level timeseries at Stations 1, 2, 3, 4, 5, and 6. Lines with and without symbols represent observed and simulated water levels, respectively.

Figure 5: The calibrated depth averaged velocity timeseries at Stations 1, 2, 3, 4, 5 and 6. Lines with and without symbols represent observed and simulated velocities, respectively. The dashed gray horizontal line marks zero velocity. Flood and ebb velocities are negative and positive, respectively.

Figure 6: Time series showing the observed and simulated dye tracer response at Stations 1, 2, 3, 3 grab, 5 grab, 6, 7 and 8. Lines with and without symbols represent the observed and modeled data, respectively. The dashed gray line represents the water level time series for each station. A black tick mark highlights the timing of the dye release. All y-axis have a consistent scale and concentrations greater than 200 ppb are out of the plot boundary.

Figure 7: Images of the simulated dye tracer plume (a) at 18:00 GMT or three hours before high tide and (b) at 19:00 GMT or two hours before high tide. Warm and cool colors represent high and low dye concentrations, respectively. Concentrations are superimposed onto the -0.79m - 0.20m intertidal creek contour. The red line marks the location of the dye release. Water levels over the tidal cycle are shown in the upper right corner and the red arrow coincides with the time of the dye map.

Figure 8: Ortho-rectified aerial photograph taken at 19:32 GMT during the field dye tracer experiment. Areas of bright and lighter shades of red represent high and low concentrations, respectively. The red line marks the location of the dye release.

Figure 9: Images of the simulated dye tracer plume (a) at 22:00 GMT two hours after high tide and (b) at 23:00 GMT three hours after high tide. Warm and cool colors represent high and low dye concentrations, respectively. Concentrations are superimposed onto the -0.79m - 0.20m intertidal creek contour. The red line marks the location of the dye release. Water levels over the tidal cycle are shown in the upper right corner and the red arrow coincides with the time of the dye map.

Figure 10: A series of maps showing the free surface elevation at 0.33hr intervals during the spring flood tide. Warm and cool colors represent high and low water surface elevation, respectively.

Figure 11: A series of maps showing the free surface elevation at 0.33hr intervals on the spring ebb tide. Warm and cool colors represent high and low water surface elevation, respectively.

Figure 12: Station 1 velocity-stage relationship from observed and modeled data. The black and blue dots represent observed and simulated values, respectively. Flood values are negative.

Figure 13: Flow vectors for the (a) flood and (b) ebb cycles of the spring tide. The vectors highlight clockwise and counterclockwise flow paths across the marsh interior during respective flood and ebb cycles.

Figure 14: Velocity vector time series from dogleg creeks 1 and 2. Red and black vectors represent the north/south and east/west sections, respectively. An inset is provided to illustrate the topographic structure of each creek. White circles mark the east/west and north/south points in the doglegs. Water levels are superimposed as a dashed blue line.

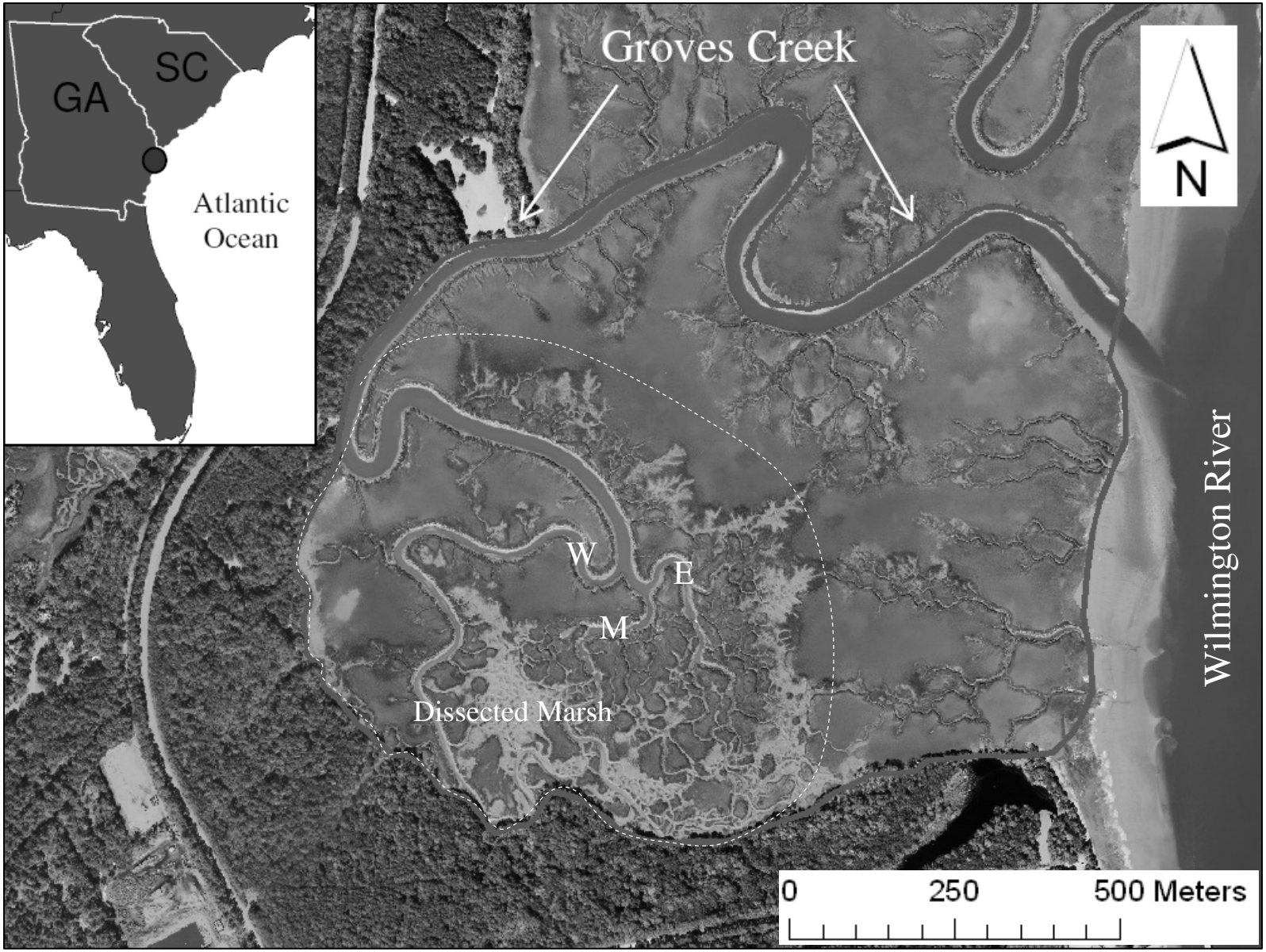
GA
SC
Atlantic Ocean
Groves Creek
N
W
E
M
Dissected Marsh
Wilmington River
0
250
500 Meters

1.

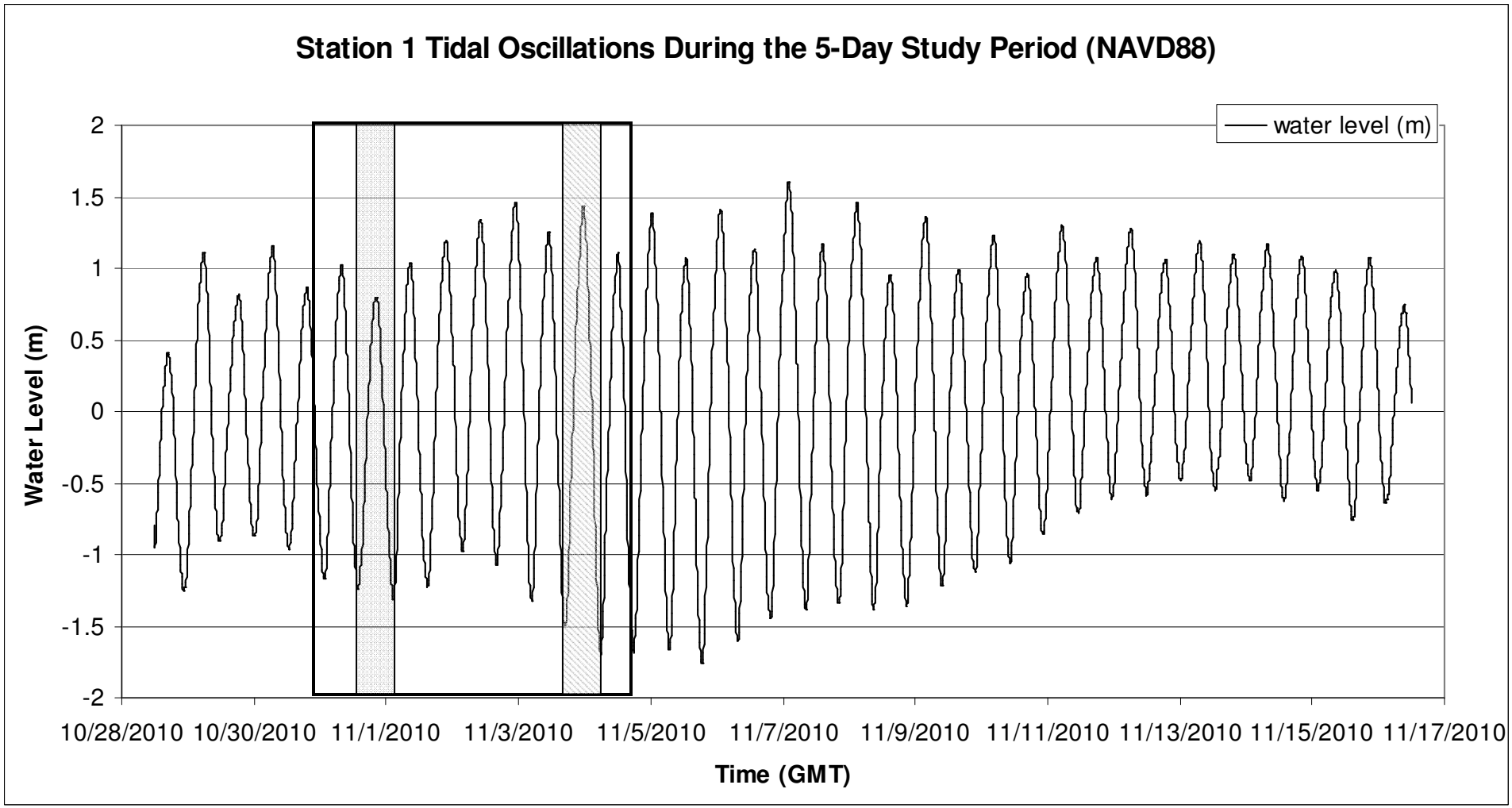
Station 1 Tidal Oscillations During the 5-Day Study Period (NAVD88)
water level (m)
Water Level (m)
2
1.5
1
0.5
0
-0.5
-1
-1.5
-2
10/28/2010
10/30/2010
11/1/2010
11/3/2010
11/5/2010
11/7/2010
11/9/2010
11/11/2010
11/13/2010
11/15/2010
11/17/2010
Time (GMT)

2.

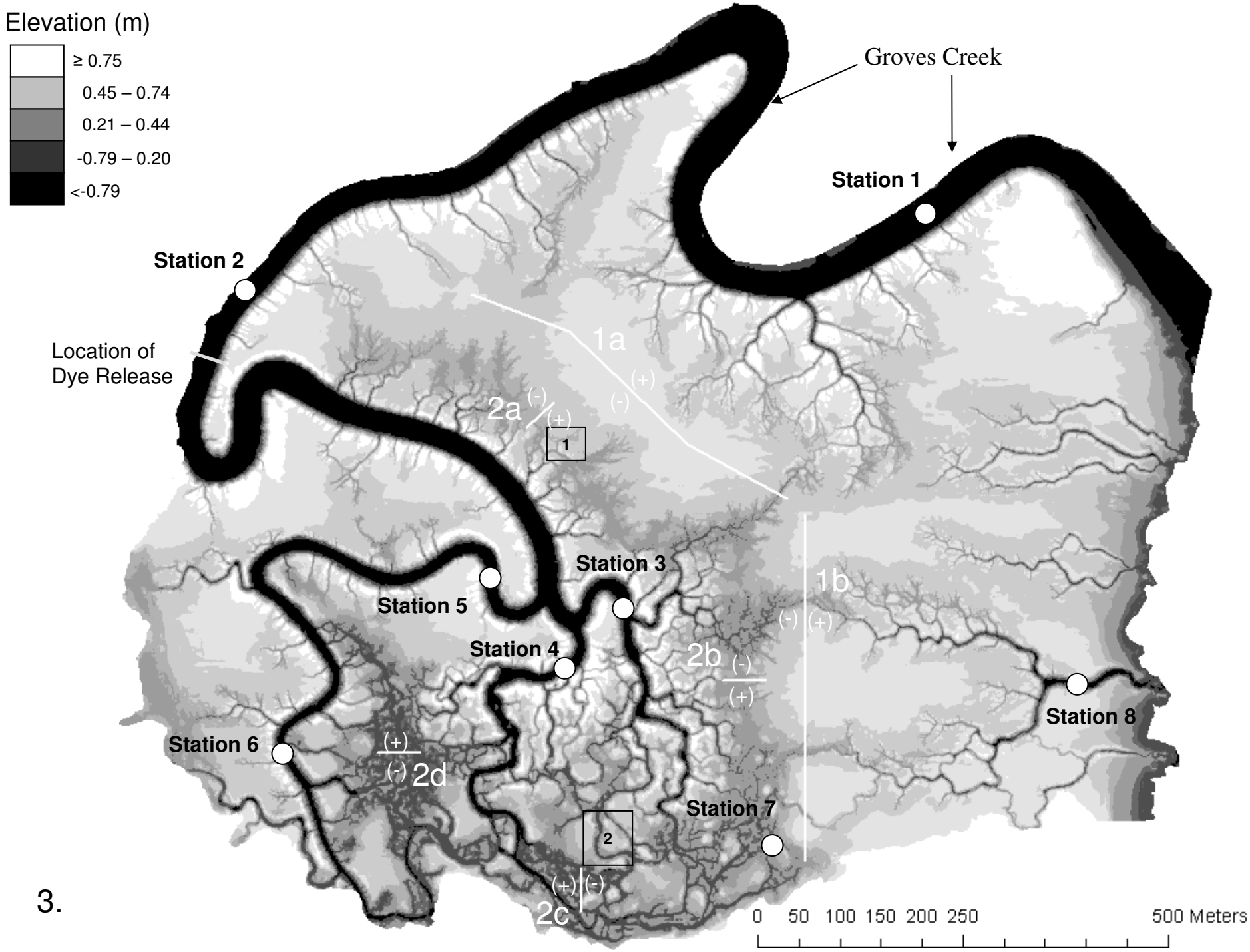
Elevation (m)
≥ 0.75
0.45 – 0.74
0.21 – 0.44
-0.79 – 0.20
<-0.79
Groves Creek
Station 1
Station 2
Location of
Dye Release
1a
(+)
(-)
2a
(-)
(+)
1
Station 3
Station 5
Station 4
1b
(-)
(+)
2b
(-)
(+)
Station 8
Station 6
(+)
(-)
2d
Station 7
2
(+)
(-)
2c
0 50 100 150 200 250 500 Meters

3.

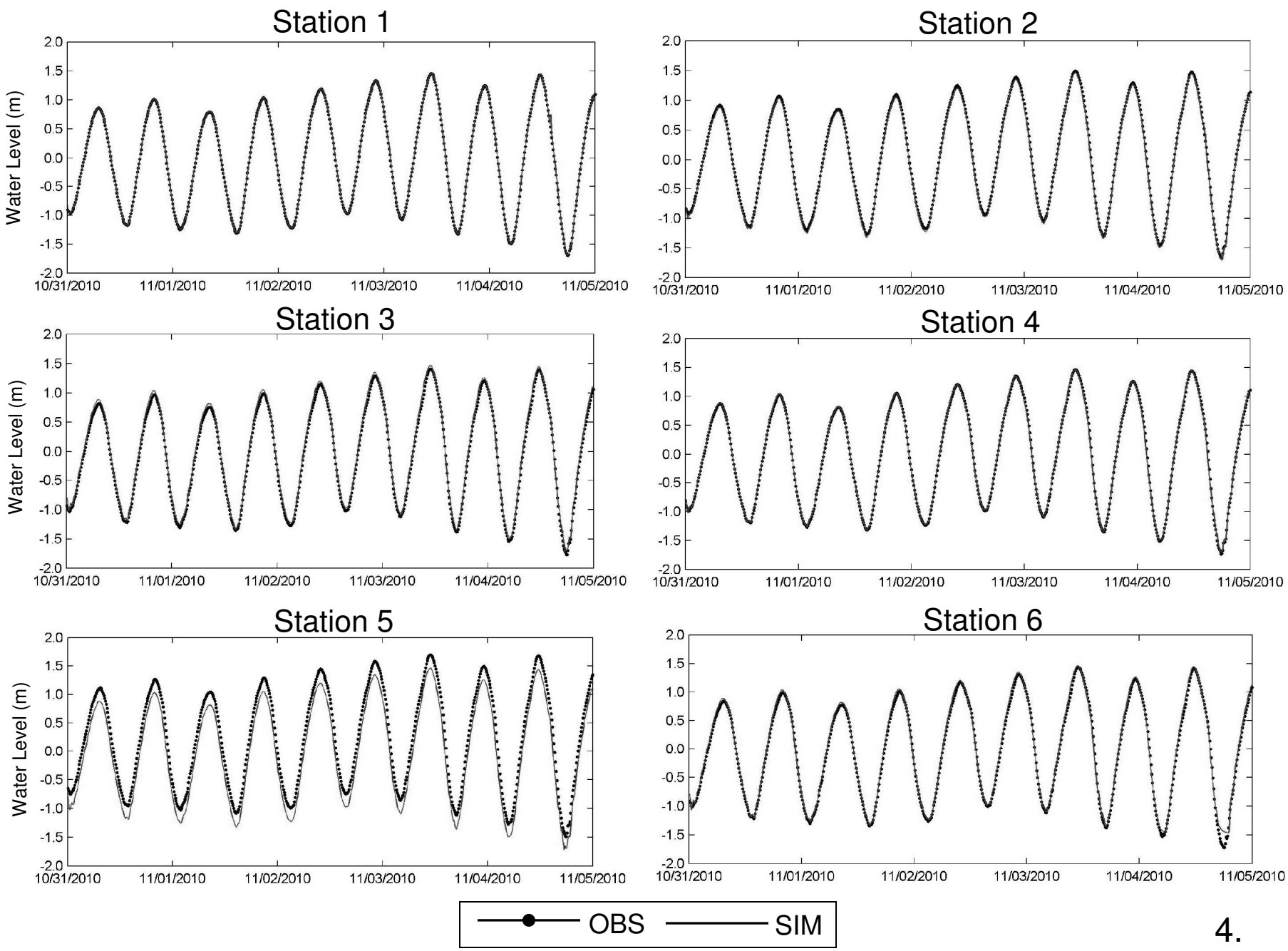
Station 1
Station 2
Station 3
Station 4
Station 5
Station 6
Water Level (m)
2.0
1.5
1.0
0.5
0.0
-0.5
-1.0
-1.5
-2.0
10/31/2010
11/01/2010
11/02/2010
11/03/2010
11/04/2010
11/05/2010
OBS
SIM

4.

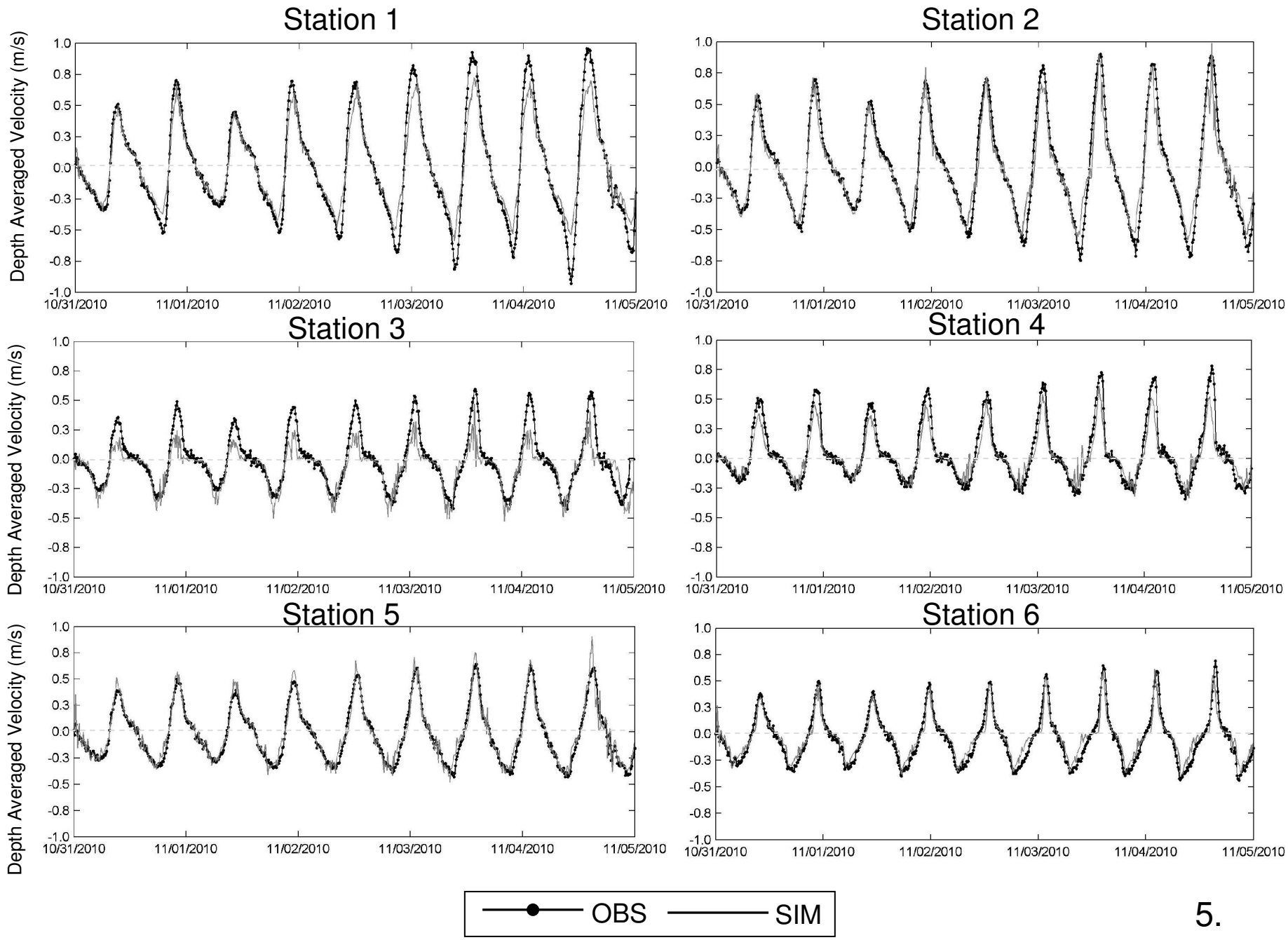
Station 1
Station 2
Station 3
Station 4
Station 5
Station 6
Depth Averaged Velocity (m/s)
1.0
0.8
0.5
0.3
0.0
-0.3
-0.5
-0.8
-1.0
10/31/2010
11/01/2010
11/02/2010
11/03/2010
11/04/2010
11/05/2010
OBS
SIM

5.

Observed and Simulated Dye Response

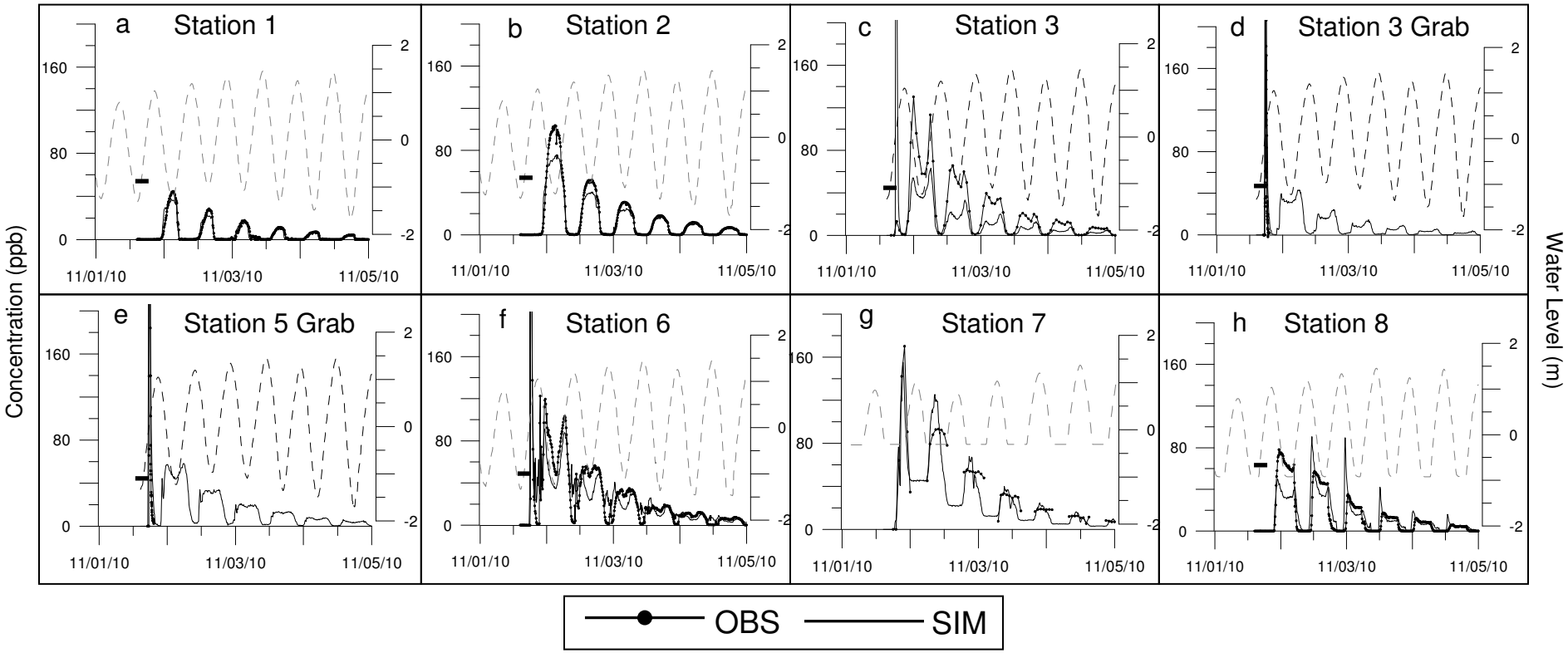

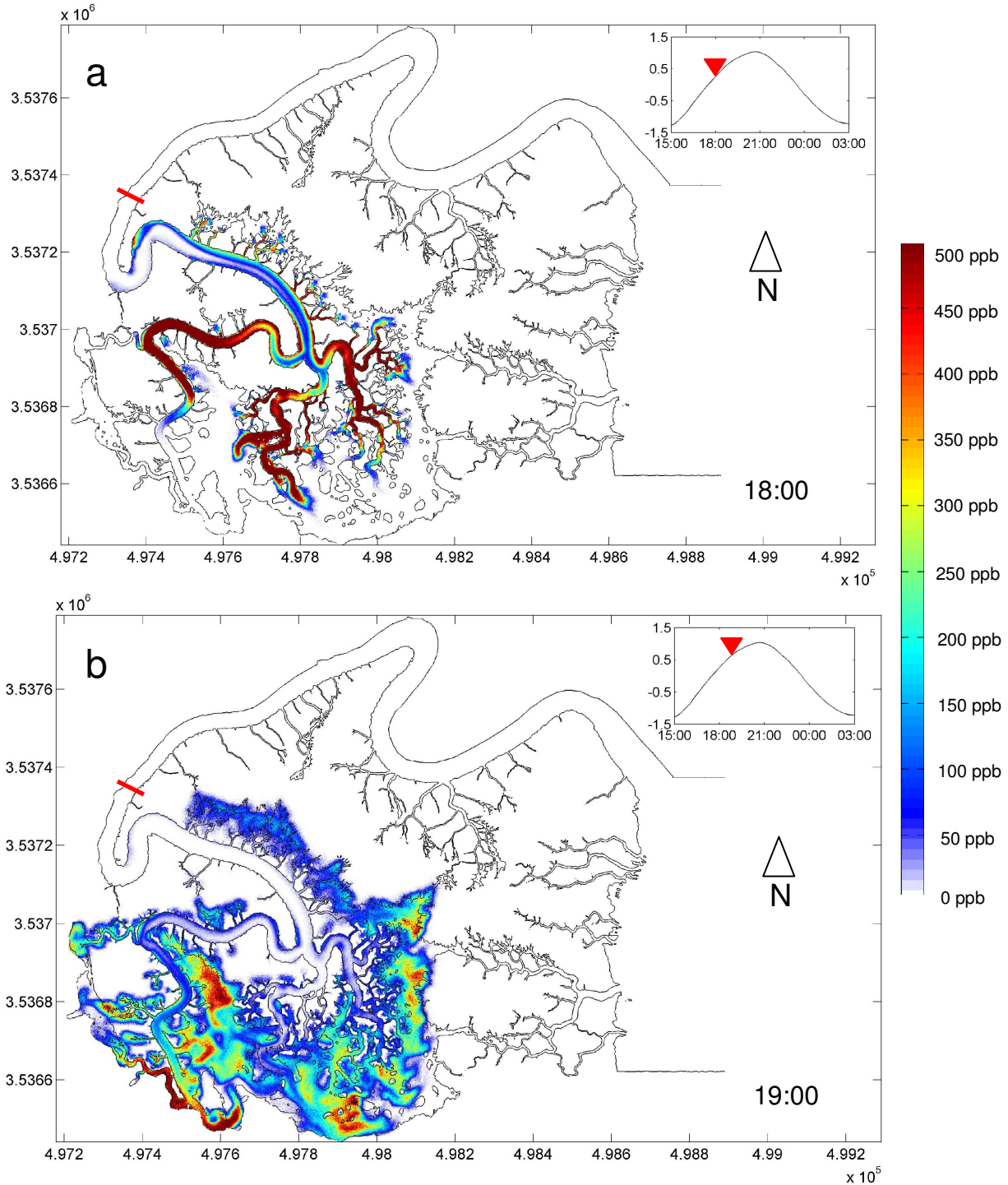
a
b
18:00
19:00
N
N
x 10^6
x 10^5
3.5376
3.5374
3.5372
3.537
3.5368
3.5366
4.972
4.974
4.976
4.978
4.98
4.982
4.984
4.986
4.988
4.99
4.992
1.5
0.5
-0.5
-1.5
15:00
18:00
21:00
00:00
03:00
500 ppb
450 ppb
400 ppb
350 ppb
300 ppb
250 ppb
200 ppb
150 ppb
100 ppb
50 ppb
0 ppb

7.

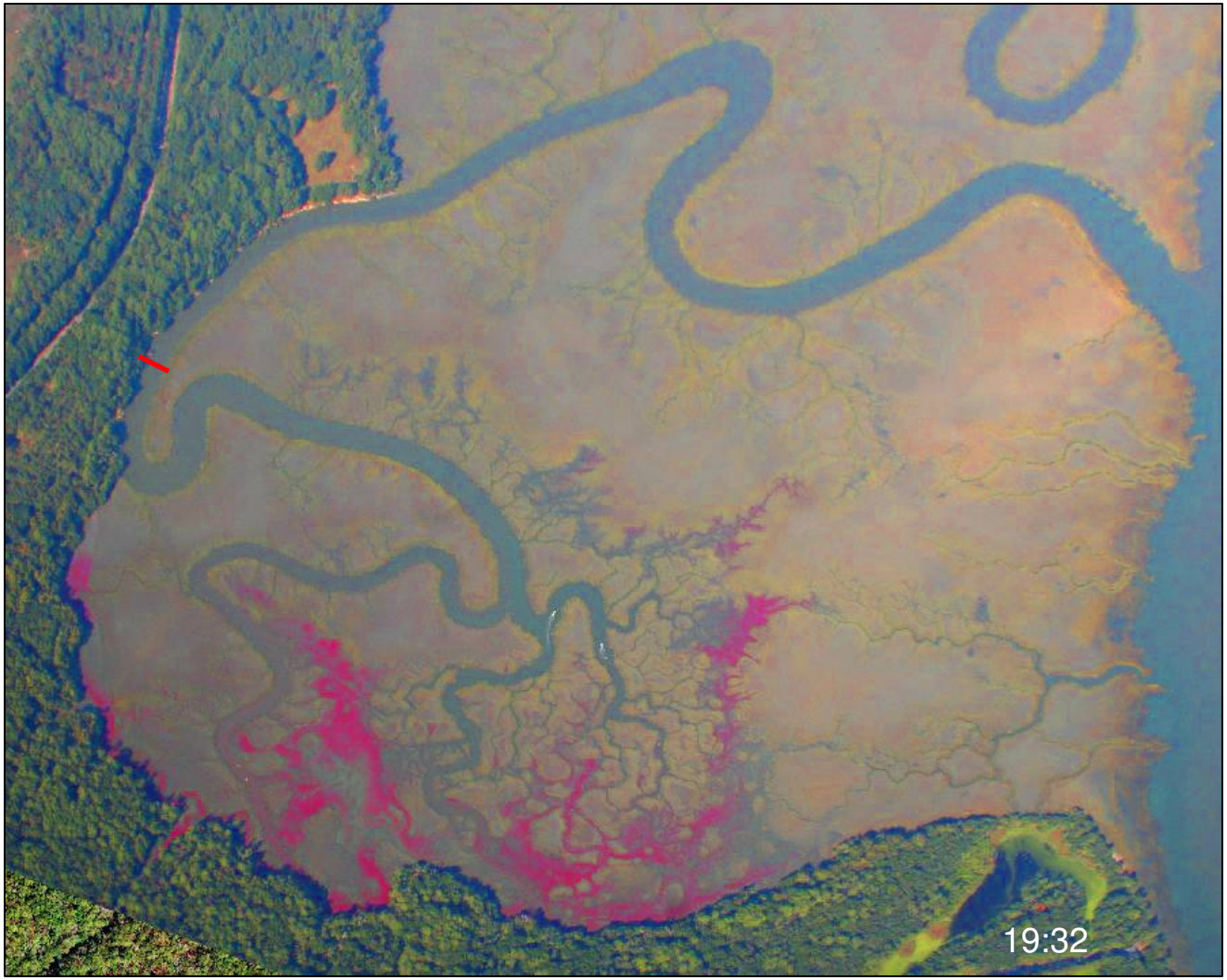
19:32

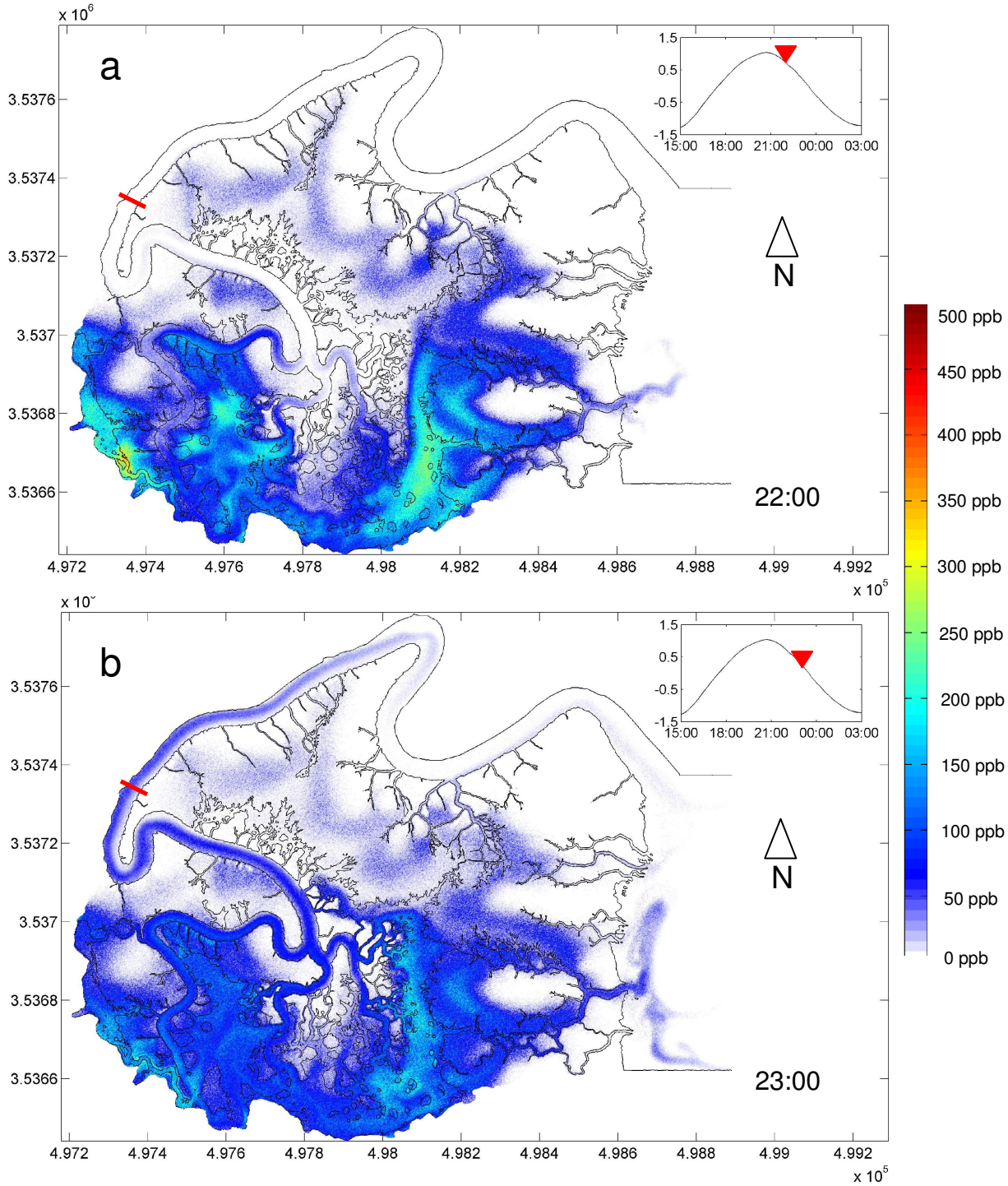
a
b
22:00
23:00
N
N
x 10^6
x 10^5
3.5376
3.5374
3.5372
3.537
3.5368
3.5366
4.972
4.974
4.976
4.978
4.98
4.982
4.984
4.986
4.988
4.99
4.992
1.5
0.5
-0.5
-1.5
15:00
18:00
21:00
00:00
03:00
500 ppb
450 ppb
400 ppb
350 ppb
300 ppb
250 ppb
200 ppb
150 ppb
100 ppb
50 ppb
0 ppb

9.

11/4/2010 – Flood Initial DEM

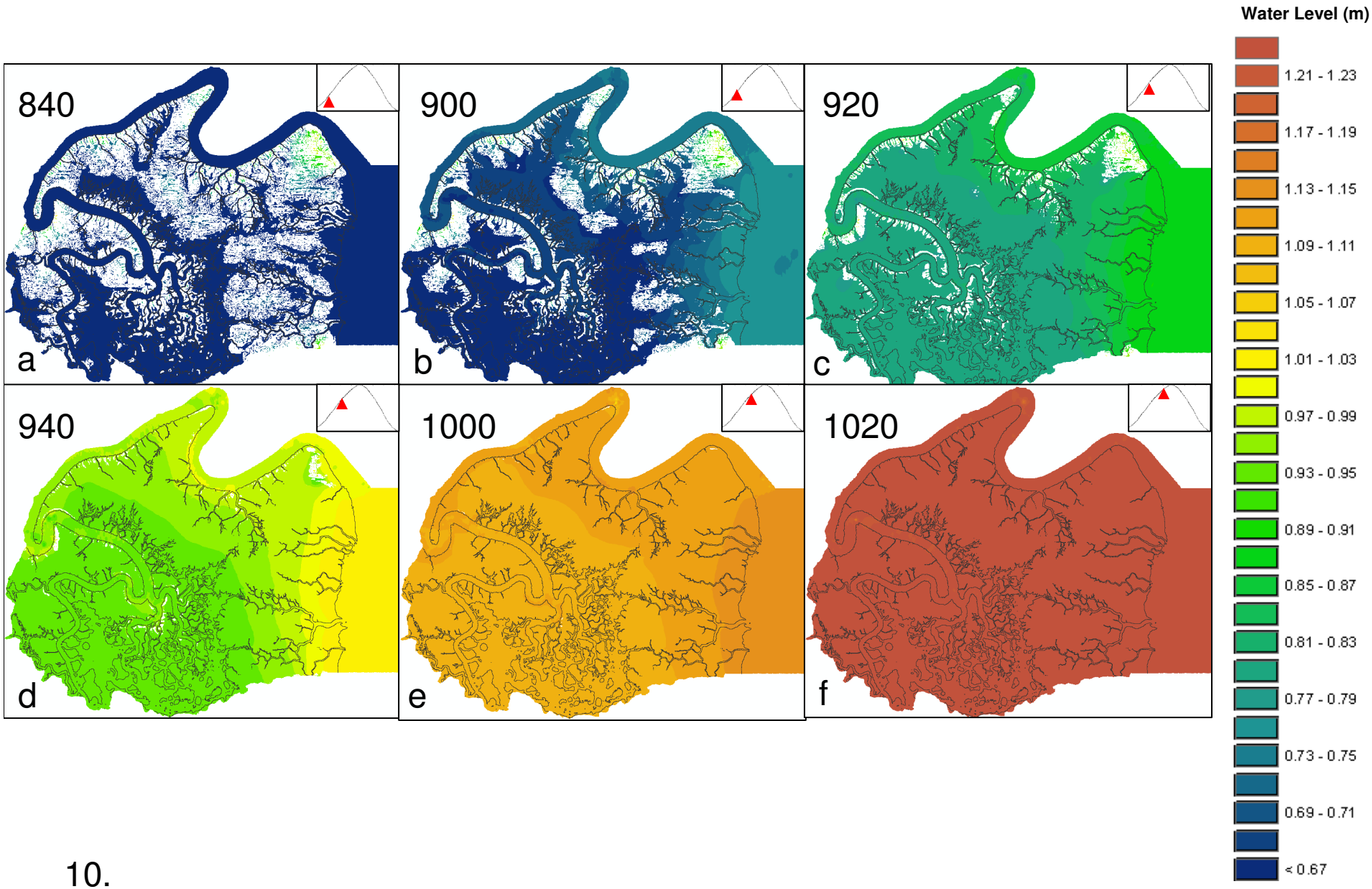

11/4/2010 – Ebb Initial DEM

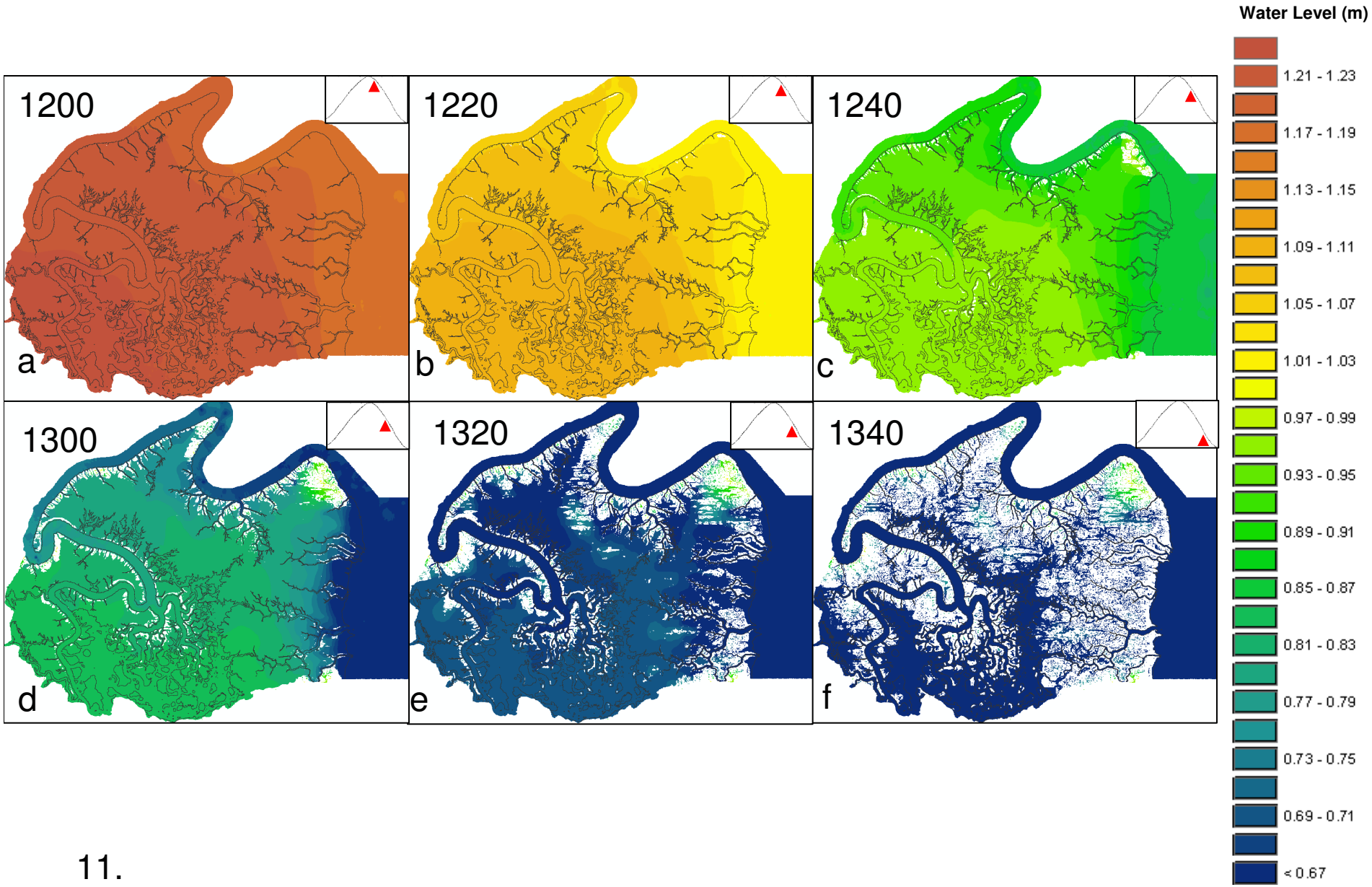

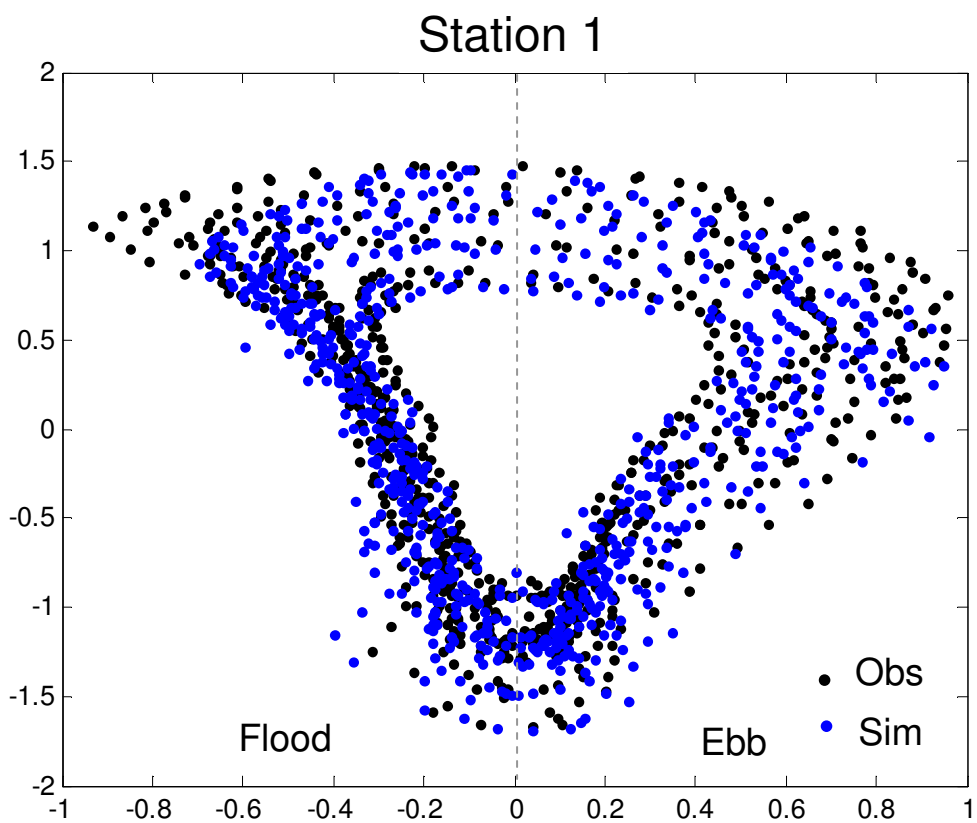
Station 1
2
1.5
1
0.5
0
-0.5
-1
-1.5
-2
-1
-0.8
-0.6
-0.4
-0.2
0
0.2
0.4
0.6
0.8
1
Flood
Ebb
Obs
Sim

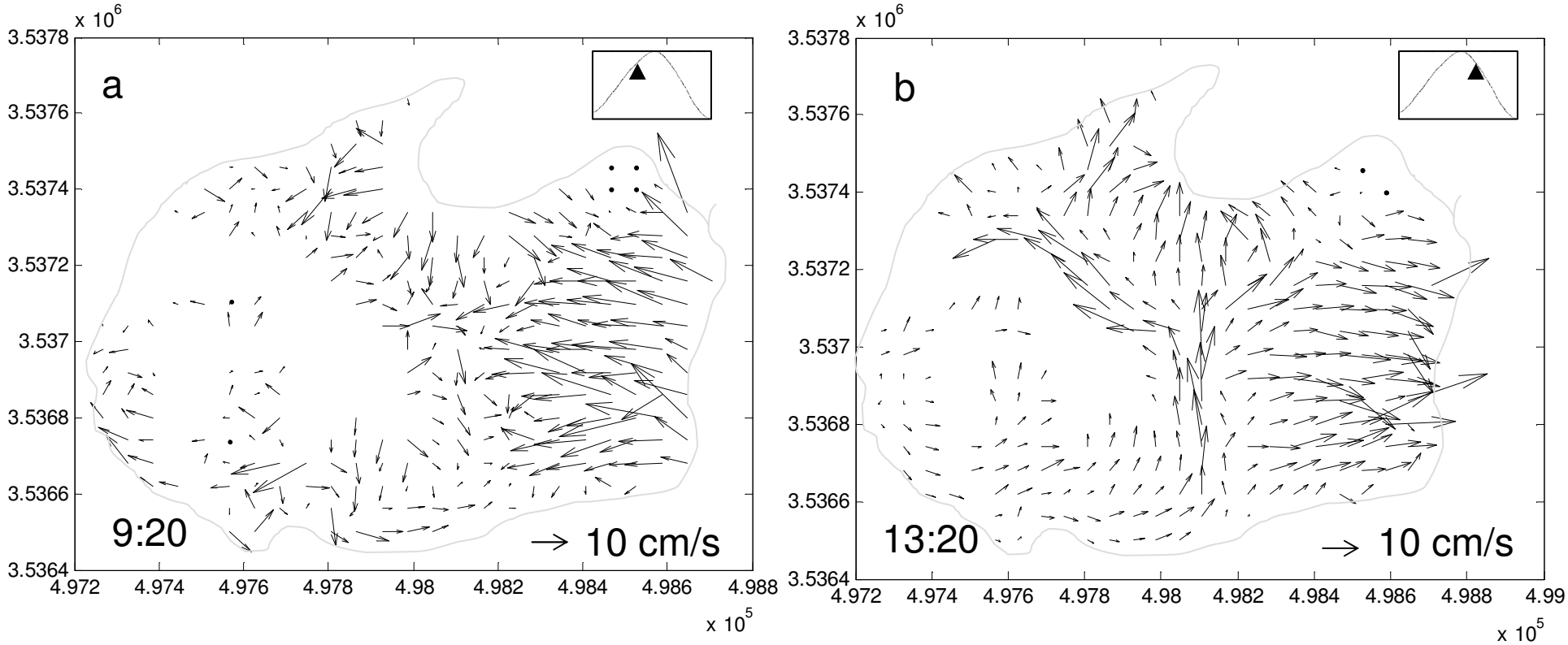
a
9:20
→ 10 cm/s
b
13:20
→ 10 cm/s
x 10^6
x 10^5
3.5378
3.5376
3.5374
3.5372
3.537
3.5368
3.5366
3.5364
4.972
4.974
4.976
4.978
4.98
4.982
4.984
4.986
4.988
4.99

13.

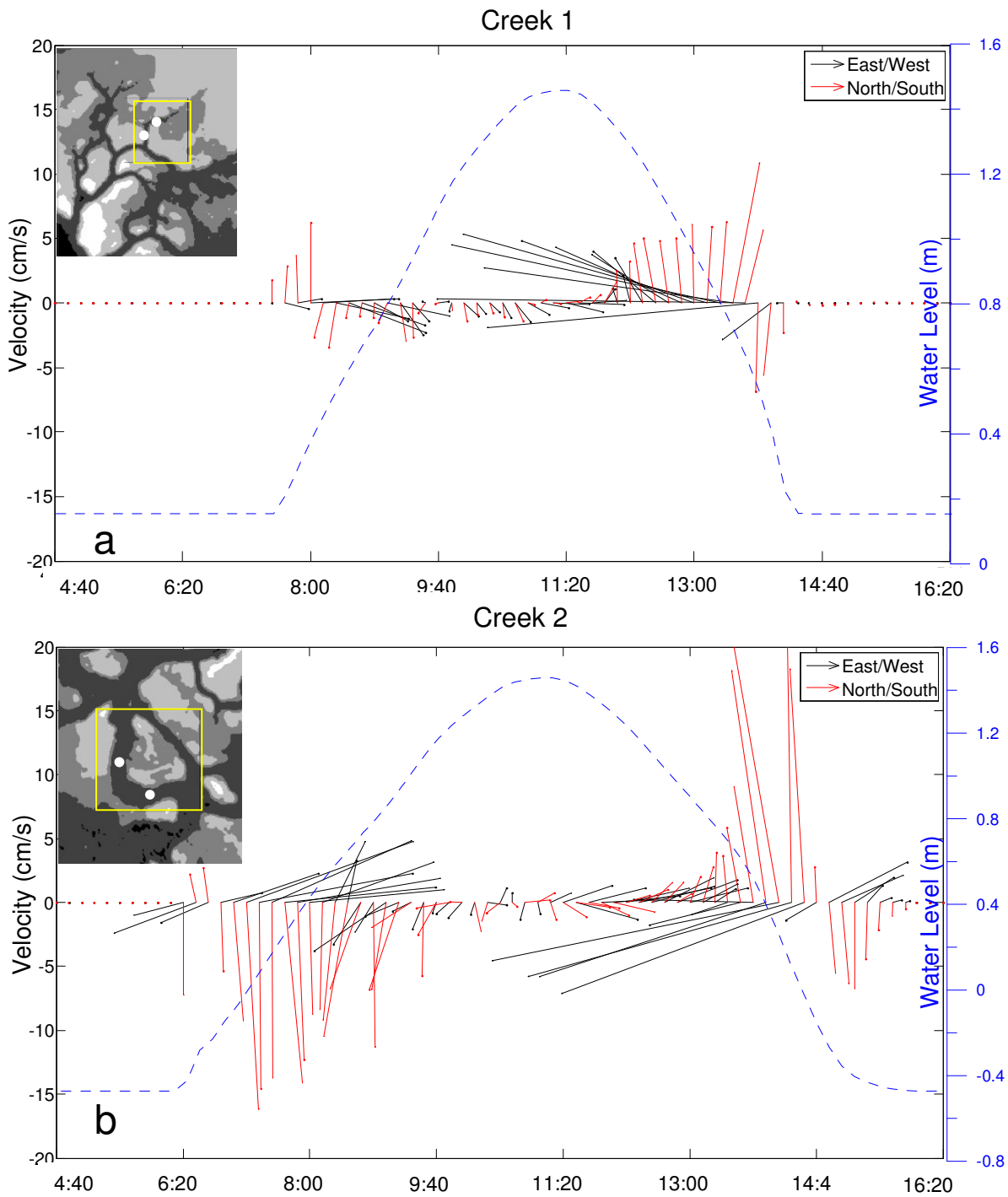
Creek 1
East/West
North/South
Velocity (cm/s)
Water Level (m)
a
4:40
6:20
8:00
9:40
11:20
13:00
14:40
16:20
Creek 2
East/West
North/South
Velocity (cm/s)
Water Level (m)
b
4:40
6:20
8:00
9:40
11:20
13:00
14:4
16:20

Grab Sample Station Dye Response (11/1/10)

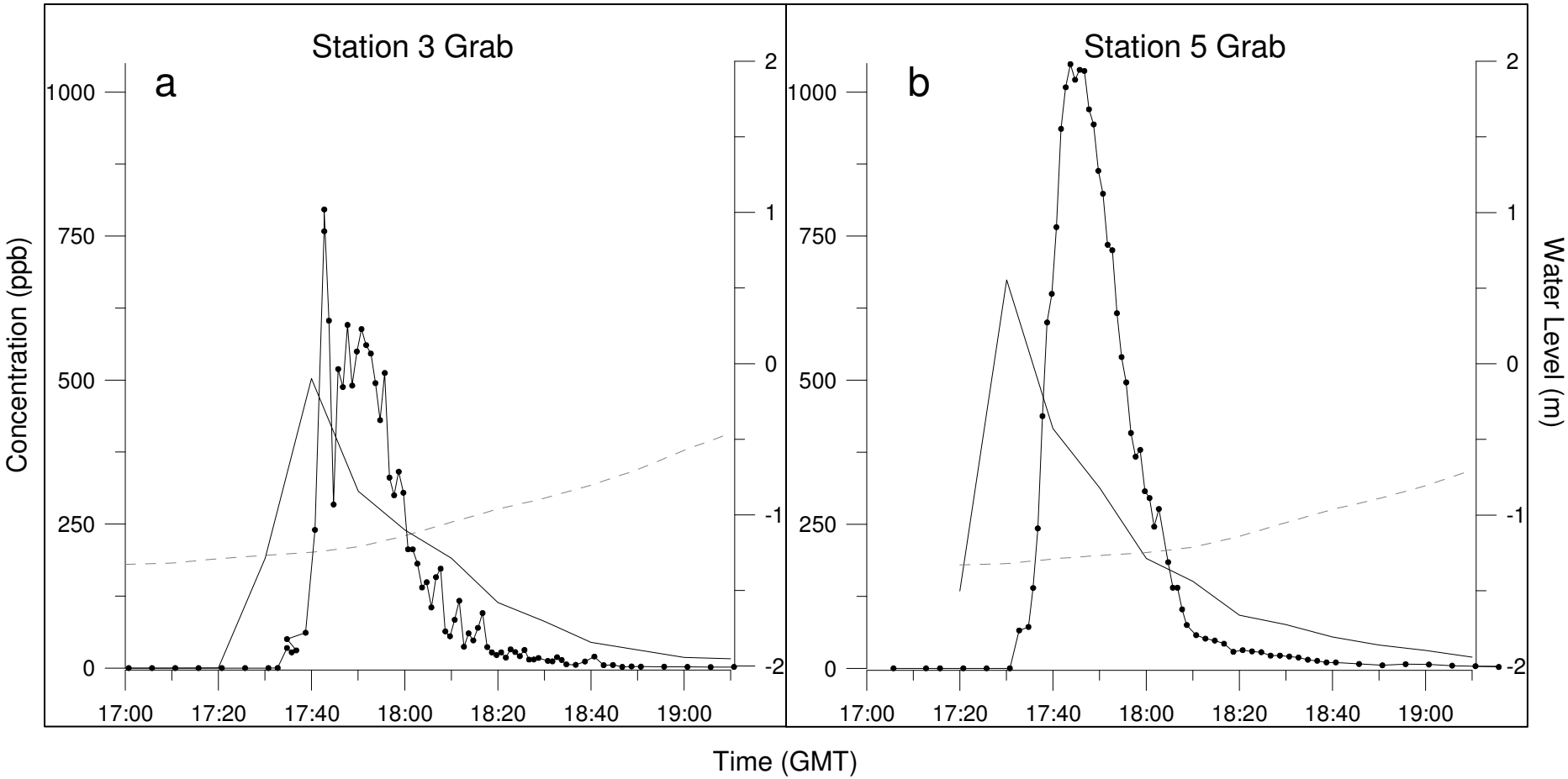

Appendix